iScience

CellPress
OPEN ACCESS

Article

A KO mouse model for the lncRNA Lhx1os produces motor neuron alterations and locomotor impairment

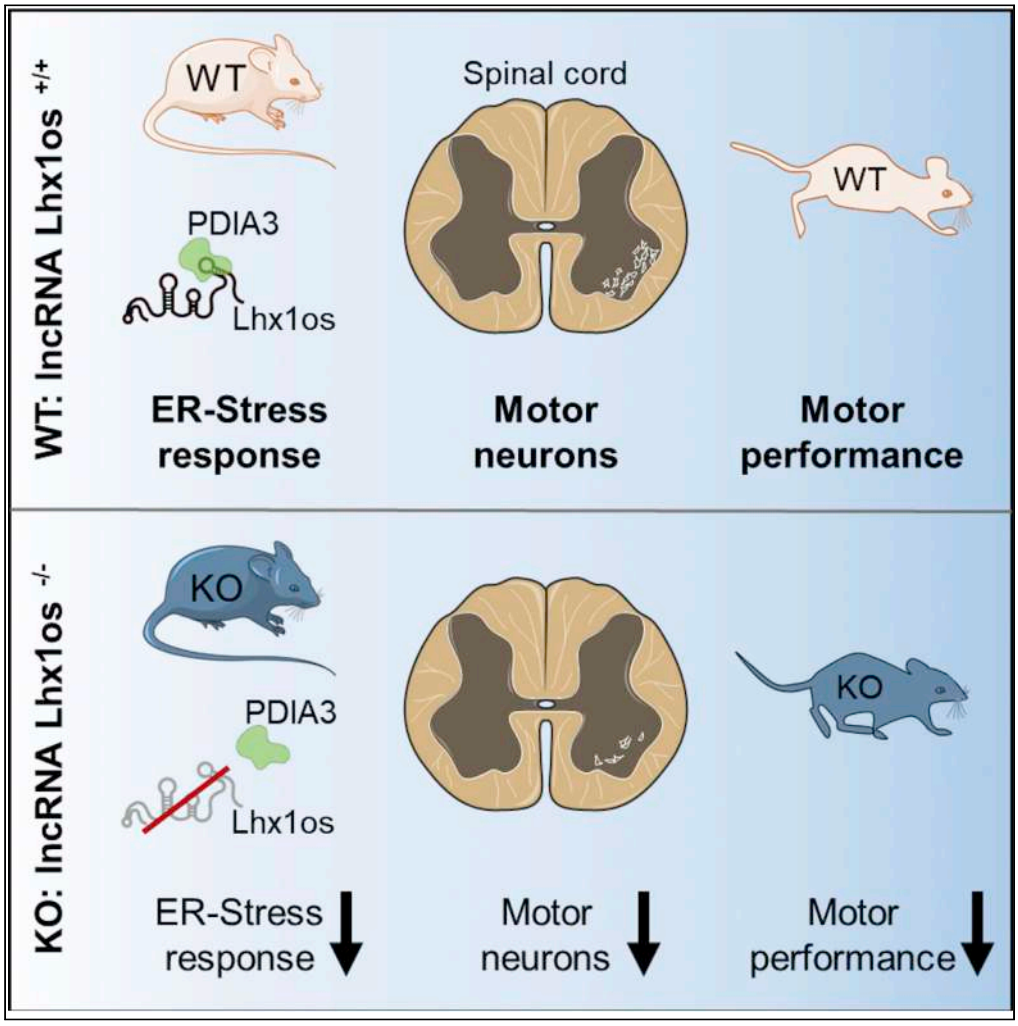

Flaminia Pellegrini, Vittorio Padovano, Silvia Biscarini, ..., Elvira De Leonibus, Julie Martone, Irene Bozzoni

julie.martone@cnr.it (J.M.)
irene.bozzoni@uniroma1.it (I.B.)

Highlights

Lhx1os is a motor neuron (MN)-specific long non-coding RNA

The Lhx1os KO mice show locomotor impairment and postnatal reduction of spinal MNs

Lhx1os is upregulated upon ER stress induction

Lhx1os interacts with PDIA3 to modulate the unfolded protein response

Pellegrini et al., iScience 26, 105891
January 20, 2023
https://doi.org/10.1016/j.isci.2022.105891

iScience

CellPress
OPEN ACCESS

Article

A KO mouse model for the lncRNA Lhx1os produces motor neuron alterations and locomotor impairment

Flaminia Pellegrini,[1,2,8] Vittorio Padovano,[1,2,8] Silvia Biscarini,[2] Tiziana Santini,[1,2] Adriano Setti,[1] Silvia Giulia Galfrè,[1] Valentina Silenzi,[1,2] Erika Vitiello,[3] Davide Mariani,[3] Carmine Nicoletti,[4] Giulia Torromino,[5] Elvira De Leonibus,[5,6] Julie Martone,[7,*] and Irene Bozzoni[1,2,3,9,*]

SUMMARY

Here, we describe a conserved motor neuron-specific long non-coding RNA, Lhx1os, whose knockout in mice produces motor impairment and postnatal reduction of mature motor neurons (MNs). The ER stress-response pathway result specifically altered with the downregulation of factors involved in the unfolded protein response (UPR). Lhx1os was found to bind the ER-associated PDIA3 disulfide isomerase and to affect the expression of the same set of genes controlled by this protein, indicating that the two factors act in conjunction to modulate the UPR. Altogether, the observed phenotype and function of Lhx1os indicate its important role in the control of MN homeostasis and function.

INTRODUCTION

In the last two decades, the identification and molecular characterization of long non-coding RNAs (lncRNAs) allowed to broaden the knowledge of the regulatory mechanisms underlying many biological processes in physiological and pathological conditions.[1] Despite commonly defined as non-abundant,[2,3] feature that made their discovery very challenging, the advent of high throughput and single cell NGS techniques unveiled that specific lncRNAs can be expressed at well detectable levels in specific cellular subtypes.[4] Moreover, their low evolutionary conservation has made their study quite laborious.[5–8]

Among the non-ubiquitously expressed lncRNAs, 40% are specific of the CNS,[9] and their roles became the subject of numerous studies in recent years.[10] Representative examples of lncRNA functions *in vivo* are the neural-specific lncRNA *Pinky* (*Pnky*) that regulates neurogenesis from neural stem cells in both the embryonic and postnatal brain;[10] the nervous system-specific Evf2 non-coding RNA that controls development of GABAergic interneurons determining GABA-dependent connectivity in the adult brain[11] or the lncRNA Synage involved in the regulation of synaptic stability and function during cerebellar development.[12] In line with their role in development, some lncRNAs have been linked to neurodegenerative diseases such as Parkinson, Alzheimer, or Huntington.[13,14]

Motor neurons (MNs) are located in the motor cortex, brainstem, and spinal cord, and project their axons into the brainstem, spinal cord, and muscles where they control movement.[15] Some lncRNAs have been specifically involved in motor neuron (MN) development and disease, such as amyotrophic lateral sclerosis (ALS) and spinal muscular atrophy (SMA), not only in mammals[16–18] but also in other model systems such as *Drosophila melanogaster* and zebrafish.[19–21] A few lncRNAs regulate transcription factors (TF) important for MNs development. Among them, the lncRNA Meg3 was found enriched in mouse embryonic stem cell-derived motor neurons and was demonstrated to scaffold PRC2/Jaird2 to maintain the silenced H3K27me3 epigenetic landscape of MN progenitors and caudal Hox genes.[22] Another lncRNA acting on TF is lncrps25 that, through the regulation of Olig2 expression, plays an essential role in MNs development. Interestingly, a zebrafish knockdown model for this lncRNA showed locomotor defects.[21] More recently, the long non-coding RNA lncMN2 was shown to promote MN maturation acting as a sponge for miR-466i-5p and upregulating targets involved in MN differentiation and function.[23] Along the same line, several lncRNAs have been associated with ALS disease (NEAT1,[24] C9orf72-AS,[25] and ATXN2-AS[26]) while others were found deregulated in blood samples derived from patients with ALS[27] or in loss-of-function *in-vitro*-derived FUS MNs.[28] Moreover, a lncRNA, SMN1-AS, was mechanistically involved in SMA acting as transcriptional repressor of the survival motor neuron protein by mediating the recruitment of the PRC2 complex on its promoter.[18]

[1]Department of Biology and Biotechnologies "Charles Darwin", Sapienza University of Rome, 00185 Rome, Italy

[2]Center for Life Nano- & Neuro-Science@Sapienza of Istituto Italiano di Tecnologia (IIT), 00161 Rome, Italy

[3]Center for Human Technologies (CHT) Istituto Italiano di Tecnologia (IIT), 16152 Genova, Italy

[4]DAHFMO - Section of Histology and Medical Embryology, Sapienza University of Rome, 00185 Rome, Italy

[5]Institute of Cellular Biology and Neurobiology "ABT", CNR, Monterotondo, 00015 Rome, Italy

[6]Telethon Institute of Genetics and Medicine (TIGEM), Pozzuoli, 80078 Naples, Italy

[7]Institute of Molecular Biology and Pathology, CNR, 00185 Rome, Italy

[8]These authors contributed equally

[9]Lead contact

*Correspondence: julie.martone@cnr.it (J.M.), irene.bozzoni@uniroma1.it (I.B.)

https://doi.org/10.1016/j.isci.2022.105891

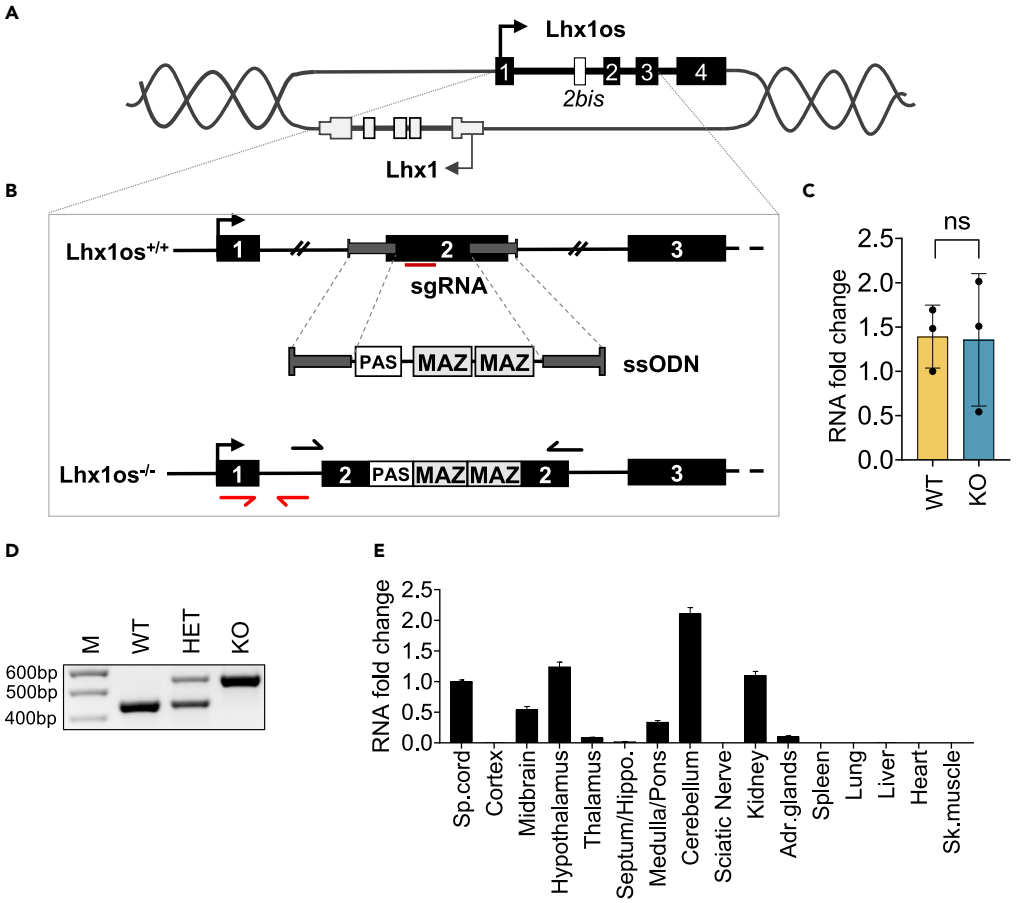
A
Lhx1os
1
2
3
4
2bis
Lhx1
B
Lhx1os+/+
1
2
3
sgRNA
PAS
MAZ
MAZ
ssODN
Lhx1os-/-
1
2
PAS
MAZ
MAZ
2
3
C
ns
RNA fold change
2.5
2.0
1.5
1.0
0.5
0.0
WT
KO
D
M
WT
HET
KO
600bp
500bp
400bp
E
RNA fold change
2.5
2.0
1.5
1.0
0.5
0.0
Sp.cord
Cortex
Midbrain
Hypothalamus
Thalamus
Septum/Hippo.
Medulla/Pons
Cerebellum
Sciatic Nerve
Kidney
Adr.glands
Spleen
Lung
Liver
Heart
Sk.muscle

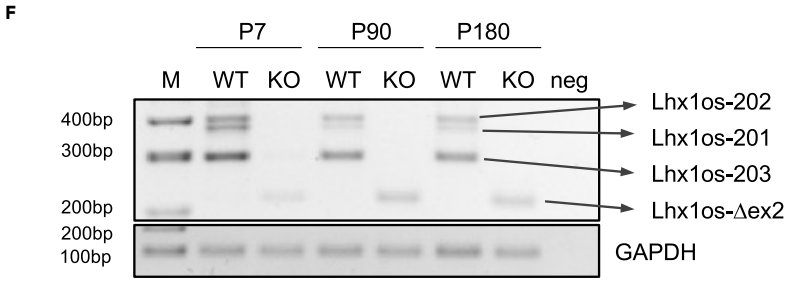
F
P7
P90
P180
M
WT
KO
WT
KO
WT
KO
neg
400bp
300bp
200bp
200bp
100bp
Lhx1os-202
Lhx1os-201
Lhx1os-203
Lhx1os-Δex2
GAPDH

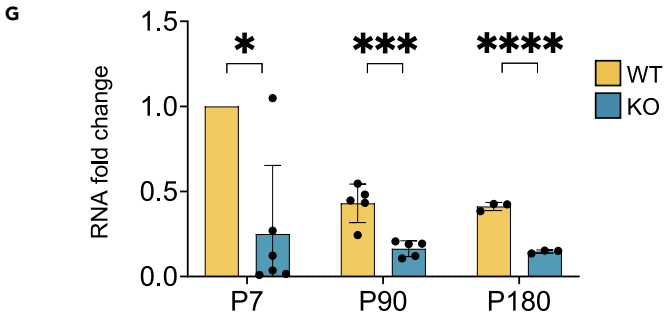
G
RNA fold change
1.5
1.0
0.5
0.0
*
***
****
WT
KO
P7
P90
P180

Figure 1. Generation of Lhx1os$^{-/-}$ mouse model

(A) Schematic representation of the Lhx1 mouse genomic locus including the Lhx1os divergent transcript.

(B) Schematic representation of the CRISPR/cas9 strategy used to obtain the KO mouse. PAS = polyadenylation site; MAZ = Binding sites for the MAZ transcription factor (which pause Pol II and promote termination); sgRNA = single guide RNAs.

(C) qPCR showing the expression of Lhx1os precursor in spinal cord RNA samples obtained from P90 WT (n = 3) and KO (n = 3) mice using 1Fw-1Rv oligonucleotides (indicated in B, red arrows). The expression levels were normalized against the GAPDH mRNA and expressed as relative quantities with respect to the WT sample set to a value of 1. Data presented as the mean ± SD. Statistical analyses were performed using Student t-test (ns $p > 0.05$).

(D) sqRT-PCR on gDNA from WT, HET, and KO mice using the oligonucleotides shown in B) (black arrows).

(E) qRT-PCR showing the expression levels of Lhx1os from the indicated WT mouse tissues (n = 1). The error bars represent the SE of the technical replicates. The expression levels were normalized against the GAPDH mRNA and expressed as relative quantities with respect to the spinal cord sample (Sp. Cord) set to a value of 1.

(F) sqPCR showing the expression of Lhx1os isoforms in spinal cord RNA samples obtained from P7, P90, and P180 of WT, HET, and KO mice using 1Fw-4Rv oligonucleotides (indicated in Figure S1D). GAPDH was used as control. Isoforms corresponding to the obtained amplification product are indicated on the right.

(G) qPCR showing the expression levels of Lhx1os from spinal cord RNA samples obtained from P7, P90, and P180 WT, and KO mice using 3Fw-4Rv oligonucleotides (indicated in Figure S1D). For each sample type, at least 3 animals were used. The expression levels were normalized against the GAPDH mRNA and expressed as relative fold change with respect to the P7 spinal cord sample set to a value of 1. Data presented as the mean ± SD. Statistical analyses were performed using Student t-test (*$p < 0.05$, ***$p < 0.001$, ****$p < 0.0001$).

In a previous study,[28] we identified a collection of lncRNAs specifically expressed in MNs obtained upon *in vitro* differentiation of mouse embryonic stem cells (mESCs). Among them, Lhx1os resulted particularly interesting since a well-conserved syntenic locus is present in the human genome and because it is highly expressed in mouse and human MNs. Notably, its expression increased in MNs carrying mutations in the FUS protein which simulate ALS conditions.[28] In this work, we carried out the *in vivo* functional and molecular characterization of Lhx1os by raising a knockout (KO) mouse model. The resulting KO mice show locomotor deficits as well as postnatal reduction of mature MNs. The dissection of its mechanism of action indicated that Lhx1os controls the unfolded protein response (UPR), through the physical interaction with the ER-associated PDIA3 protein.

The Lhx1os RNA represents a key example of a mammalian lncRNA, conserved in human, that shows a relevant role in the control of motor neuron homeostasis *in vivo*.

RESULTS

Generation of a Lhx1os KO mouse model

The murine Lhx1os lncRNA, which originates from chromosome 11 (chr11:84,416,486-84,426,657- Genome assembly: GRCm39/mm39), is highly upregulated during *in vitro* differentiation of mESCs into MNs.[28] It is transcribed in divergent orientation to the Lhx1 gene (Figure 1A), which encodes for a transcription factor with a well-described role in early mesoderm formation and in lateral mesoderm differentiation and neurogenesis.[29–32] The two genes do not overlap, as confirmed by the reference dataset of transcription start sites[33,34] (Figure S1A), by RNA-seq reads alignment[28] and by Lhx1os 5'RACE PCR (Figure S1B).

A similar genomic organization is found in human where the Lhx1-DT transcript (chr17:36,861,674-36,936,661 – Genome Assembly: GRCh38/hg38) is also strongly upregulated in MNs derived *in vitro* from iPSCs.[28]

For the functional characterization of this lncRNA, a Lhx1os KO mouse model was generated, through CRISPR-Cas9 editing, by inserting a poly-A signal in the second exon of the gene (Figure 1B). The poly-A insertion site was selected to preserve the overall genomic structure of the locus, the proximal promoter, and TSS of the divergent Lhx1 transcript. Moreover, given that the act of transcription itself is known to impact on the transcriptional activity of adjacent loci and in particular of divergent genes,[35] we showed that through our genome editing procedure we were able to preserve the transcription of the first part of the Lhx1os gene (Figure 1C).

Several heterozygous mice (Lhx1os$^{+/-}$) were obtained from the first zygotic injection and F2 animals breeding generated homozygous mice (Lhx1os$^{-/-}$). The expected editing was confirmed by genomic PCR amplification and sequencing of the portion surrounding the homologous recombination region

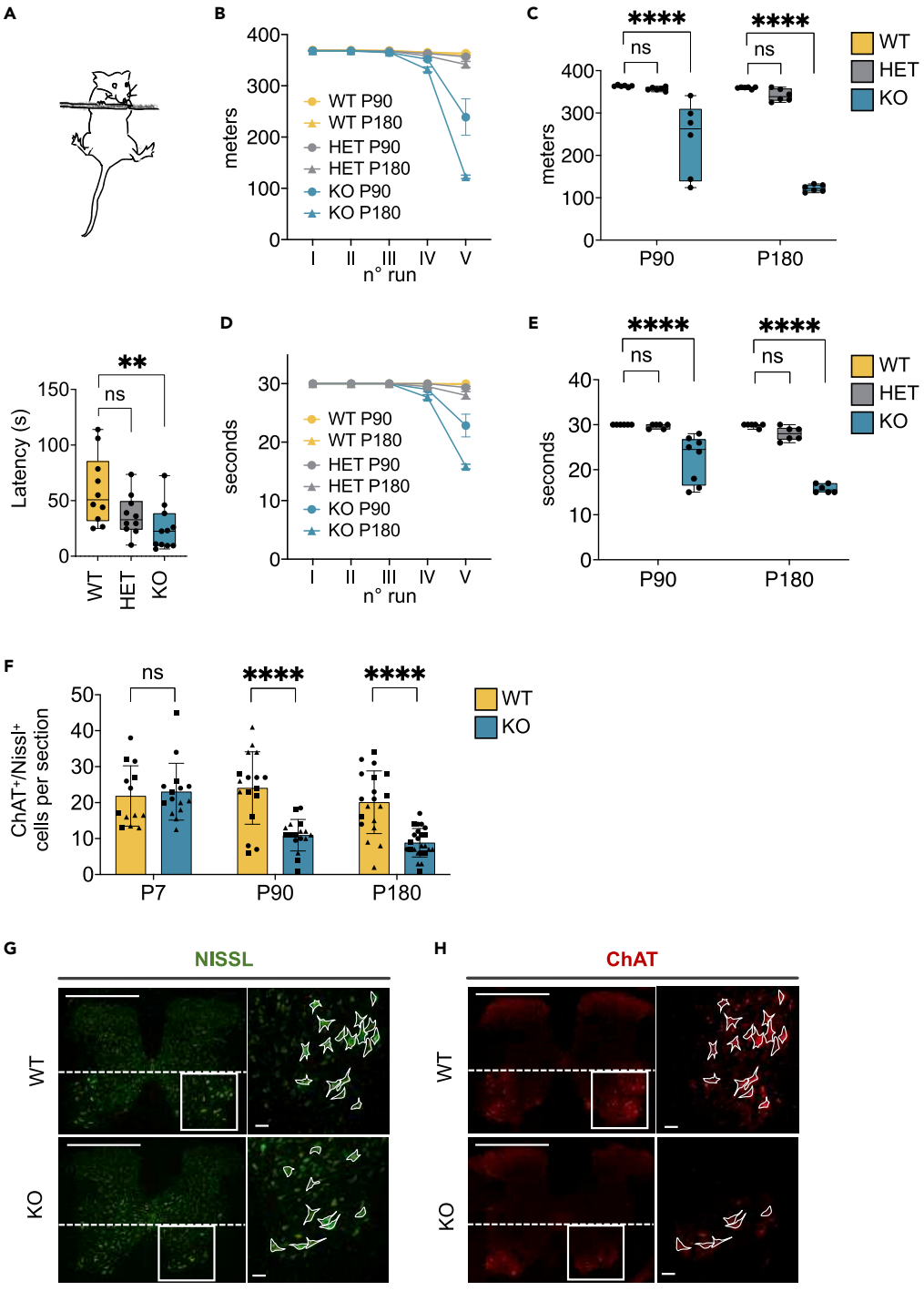

Figure 2. Differences in genetic background influence motor performance and motor neuron count in the lumbar spinal cord

(A) Hanging steel performance assessed on P90 male WT (n = 10), HET (n = 10) and KO (n = 11) mice. Data are represented as box plots and error bars span from the minimum to the maximum value. Statistical analyses were performed using one-way ANOVA followed by post-hoc Dunnett's Multiple Comparison test (ns Padj>0.05, ** Padj<0.01).

(B) Treadmill test performance represented by meters per run on the following 6 groups of mice: WT P90 (n = 6), HET P90 (n = 6), KO P90 (n = 6), WT P180 (n = 6), HET P180 (n = 6), and KO P180 (n = 6). Treadmill test was repeated twice a week for a total of five runs (I-V) and run meters and time were recorded. Values are mean ± SEM.

Figure 2. *Continued*

(C) Meters covered in the fifth run by each group of mice. Data are represented as box plots and error bars span from the minimum to the maximum value. Statistical analysis was performed through two-way ANOVA. Age-matched groups were compared by performing Bonferroni's Multiple Comparison test (ns Padj>0.05, **** Padj <0.0001).

(D) Treadmill test performance represented by minutes per run on the same animals described in (B). Values are mean ± SEM.

(E) Run time in the fifth run for each group of mice. Data are represented as box plots and error bars span from the minimum to the maximum value. Statistical analysis was performed through two-way ANOVA. Groups were compared by performing Bonferroni's Multiple Comparison test (ns Padj>0.05, **** Padj <0.0001).

(F) Quantification of motor neurons in lumbar spinal cord of WT and KO mice at the indicated ages (n = 3 animals and at least n = 5 slices/animals were analyzed). Values are mean ± SD. Each symbol (circle, triangle, or square) represents slices which belong to a single mouse. Statistical analyses were performed using two-way ANOVA. Groups were compared by performing Bonferroni's Multiple Comparison test (ns Padj>0.05, ****p < 0.0001).

(G and H) Representative spinal cord sections from P90 WT and KO male mice double-labeled with NISSL staining (G; green) and ChAT antibody (H; red). In right panels, magnification of ventral horns highlighted by white squares. Double stained cells with diameter >20 μm (marked with solid lines) were selected for MNs quantification. Scale bar: 500 μm (left panels) and 50 μm (right panels).

(Figures 1D and S1C). Lhx1os$^{-/-}$ mice were born in expected Mendelian ratios and were normally viable after birth (Table S1).

Investigation in different tissues indicated that Lhx1os expression is restricted to the nervous system (spinal cord, hypothalamus, and cerebellum) and to the kidney (Figure 1E). Analysis of the Lhx1os transcripts in the spinal cord of control mice showed the existence of three isoforms (Figure S1D), all expressed in the different postnatal stages analyzed (WT P7, P90, and P180), with the Lhx1os-203 (ENSMUST00000134800.7) transcript being the most abundant (Figure 1F).

Lhx1os$^{-/-}$ (KO) mice displayed the complete lack of the Lhx1os-annotated isoforms and a residual accumulation of a novel transcript containing exon 1 fused to exon 3 (Lhx1os-Δex2), never observed in WT controls (Figure 1F). These results were confirmed by the RNA-sequencing analyses performed on WT and KO spinal cord from P90 animals that showed a complete loss of exon 2 and only residual levels of exon 3 and exon 4 (Figure S1E). The overall amount of Lhx1os, quantified by qPCR in WT spinal cord (SC) samples taken at different stages, showed an initial decrease between P7 and P90 that remained constant until P180, while the residual amount of the aberrant Lhx1os-Δex2 transcript in the KO samples was always around 30% with respect to age-matched WT controls (Figure 1G). The amount of Lhx1os was also assessed in P90 Lhx1os$^{+/-}$ heterozygous mice where a downward trend was observed, even if not significant (Figure S1F). Interestingly, the reduction of the Lhx1os transcript had no effect on the divergent Lhx1 gene, both at the mRNA (Figure S1G) and protein (Figure S1H) levels, allowing to exclude its involvement in the transcriptional control of the adjacent divergent locus.

Lhx1os-KO mice have impaired neuromuscular capacity

Adult Lhx1os$^{+/+}$ (WT), Lhx1os$^{+/-}$ (HET), and Lhx1os$^{-/-}$ (KO) male mice were used for functional tests. The hanging steel test was performed to verify whether Lhx1os$^{-/-}$ mice manifest impaired muscular strength. We found a significant difference between P90 WT and KO animals, with a decrease in performance of 38% in HET mice and 57% in KO siblings (Figure 2A). At least 10 animals of each genotype were tested. The analyzed mice did not show genotype-related differences in body weight (Figure S2A). Notably, no significant differences between genotypes were found in general exploratory behaviors such as the open field test (WT n = 10, HET n = 10, KO n = 11; Figure S2B). To deepen the relevance of the neuromuscular deficit, mice were subjected to a locomotor exhaustion test, which was carried out by forcing the mice to run on a treadmill.[36] The test was conducted on different groups of mice at different ages (P90 and P180-days-old mice) to test whether there was an age-dependent worsening of motor performance, being careful to use at least 6 mice of each genotype and age. Both P90 and P180 groups of KO animals exhibit differences with respect to WT. The distance traveled and the running times, both measures of motor efficiency, decreased for KO animals from the fourth run onward (Figures 2B and 2D); interestingly, the magnitude of decrease in both parameters was significantly exacerbated in the older mice group (P180). In fact, while the distance traveled decreased in the fifth run of ca. 34% for P90 mice, the difference reached the 66% for P180 animals (Figure 2C). Similar alterations were observed for the running time (Figure 2E).

Differences between the WT and KO genotypes were also observed in the number of shocks which, in the initial days of training, indicates the opposition to run and, in the following days, the degree of physical exhaustion. P90 and P180 KO animals received more shocks, with respect to WT ones. This feature becomes clear from the third run and even more evident in the fifth run, where only 4 out of 6 mice from P90 and none from P180 were able to finish the run (Figure S2C, for P90 mice and Figure S2D, for P180 mice). HET animals showed no differences in the meters and time of run, while a trend of progressive increase in the number of shocks was observed (Figures S2C and S2D).

The motor phenotype of KO animals suggested an early onset of neuromuscular impairment which worsens with age.

We then wondered whether motor impairment in KO animals might be associated with MNs loss. To analyze this aspect, we performed MN counts in coronal sections of the lumbar (L1–L5) spinal cord of P7, P90, and P180-old animals. Spinal cord sections were labeled with Nissl compound and choline acetyltransferase (ChAT) antibodies, and only double-positive cells with diameter values > 20 μm were counted in the adult spinal cords (P90 and P180).[37–40] In the P7 spinal cords, the double-positive cells were counted independently of their dimensions, to avoid the exclusion of many smaller motoneurons. In fact, in adult mice, the global $ChAT^+$ cells size distribution is shifted toward higher values with respect to postnatal mice, because of postnatal growth.[41] The analysis of MNs showed no differences between WT and KO animals sacrificed at P7 (Figure 2F; representative Nissl staining and ChAT immunofluorescence are shown in Figures S3A and S3B, respectively), allowing to exclude developmental defects in MN formation or death during embryonic development.[42] Instead, the analysis at P90 showed a significant decrease in KO animals of about 56% (Figure 2F; representative Nissl staining and ChAT immunofluorescence are shown in Figures 2G and 2H, respectively) that remained constant at P180 (decrease in homozygous animals of about 60%, Figure 2F; representative Nissl staining and ChAT immunofluorescence are shown in Figures S3C and S3D, respectively). These results suggest that the reduction of MNs in KO animals occurs progressively during postnatal life and mainly between P7 and P90.

Transcriptome analysis of spinal cords from control and KO mice

To study the impact of Lhx1os loss on gene expression, we analyzed the spinal cord transcriptomes of P90 control and $Lhx1os^{-/-}$ mice. Differential expression analysis identified 70 genes, of which 61 downregulated and 9 upregulated in KO conditions (adjusted p value <0.1). These genes are listed in Table S2 and a volcano plot representing the most prominent changes in gene expression is shown in Figure S4.

We then performed a functional enrichment analysis of downregulated and upregulated genes. The Biological Process GO (Gene Ontology) terms enriched among the downregulated genes were generally associated with the ER stress (Figure 3A), while the upregulated ones identified the neuroinflammatory response (Figure 3B). Interestingly, among the downregulated genes belonging to the categories related to the ER stress response, we found several genes previously described to be activated during the UPR to protect cells from ER stress and known to be altered in ALS human postmortem spinal cords.[43] This list of genes includes i) Hspa5 (also known as BiP), a heat shock protein associated with the ER chaperone complex that is involved in a wide range of folding processes and can trigger, upon unfolded protein accumulation, UPR;[44] ii) Xbp1, another master regulator of the UPR and of the ER-associated protein degradation (ERAD) response;[45] iii) Herpud1, involved in both in UPR and ERAD[46,47]; PDIA4 and PDIA6, two disulfide isomerase (PDI) proteins of the ER that catalyze the formation and isomerization of disulfides during oxidative protein folding.

Several of these transcripts, identified in the RNAseq and linked to the ER stress response, were validated by qRT-PCR analysis on WT and KO animals (Figure 3C).

Lhx1os protein interactors

In order to find a possible functional link with these pathways, we searched for protein interactors of Lhx1os RNA by performing an UV crosslinked RAP-MS (RNA antisense purification with mass spectrometry) using whole cell lysates from mESC-derived MNs (Figure S5A). Two sets of biotin-labeled ssDNA antisense oligos, 90 nt long, were used. The first probe-set was composed by 5 non-overlapping sequences complementary to different regions of Lhx1os (Figure S5B), while the second set was composed by three sequences against the U1 small nuclear RNA (snRNA), that was used as positive control of RAP efficiency.[48] The relative enrichment of Lhx1os and U1 RNAs was assessed by qRT-PCR (Figure S5C) and protein

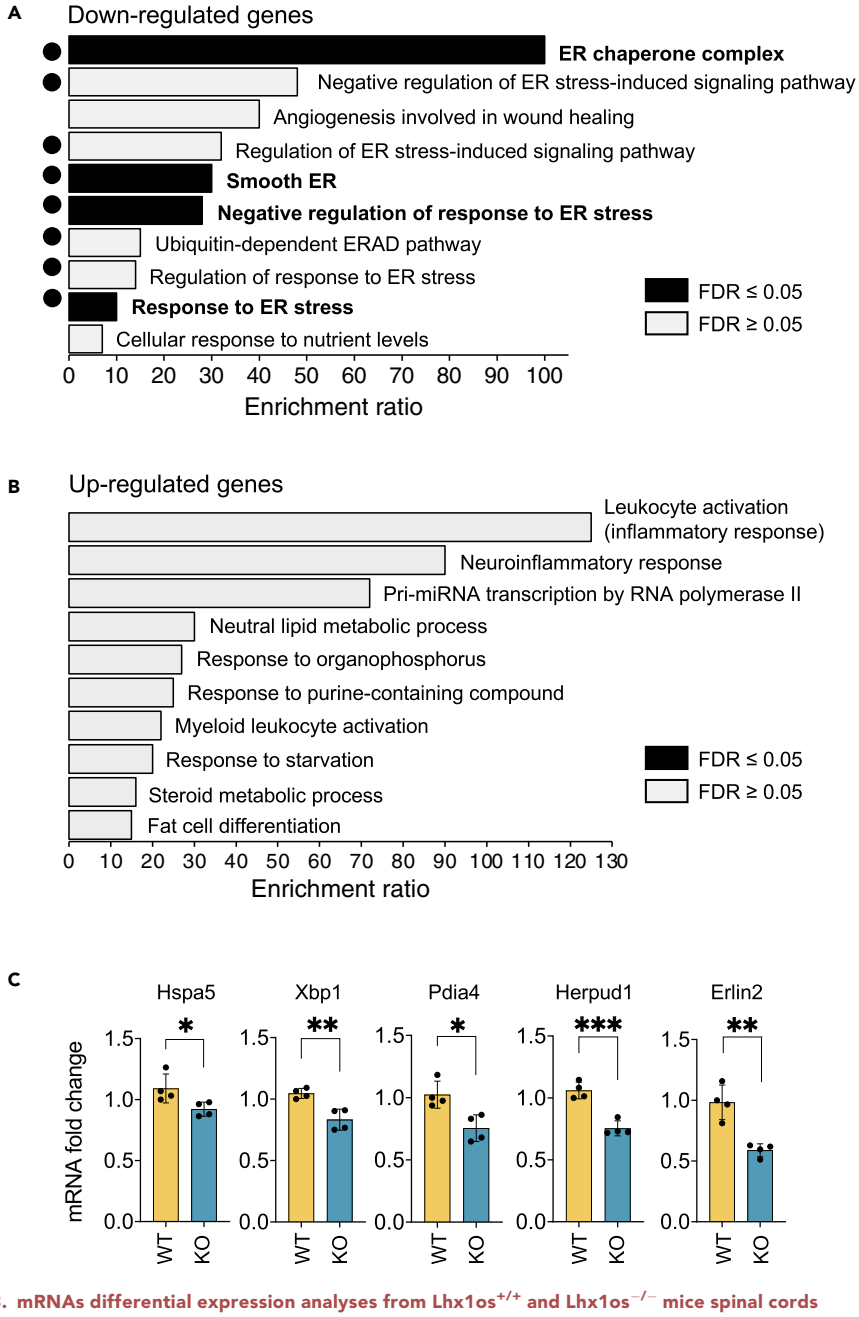

Figure 3. mRNAs differential expression analyses from Lhx1os$^{+/+}$ and Lhx1os$^{-/-}$ mice spinal cords

(A) Bar chart showing the Gene Ontology (GO) terms enrichment analysis of the downregulated genes identified by RNA-seq analysis of WT and KO spinal cords from P90 old mice. All enrichments are significant at FDR <0.05.

(B) Bar chart showing the GO terms enrichment analysis of the upregulated genes identified by RNA-seq analysis of WT and KO spinal cords from P90 mice. All enrichments are significant at FDR <0.05.

(C) qRT-PCR validations of indicated deregulated mRNAs identified in spinal cord samples by RNA seq-data from WT and KO P90 mice. The RNA expression levels in qRT-PCR analyses were normalized against GAPDH mRNA and expressed as relative quantities with respect to a WT mouse sample set to a value of 1. Data are presented as the mean ± SD of 4 mice for each group. Statistical analyses were performed using Student *t*-test (*p < 0.05, **p < 0.01, ***p < 0.001).

samples were analyzed by mass spectrometry. 48 proteins resulted to be enriched in the Lhx1os immunoprecipitated sample (Lhx1os/U1 ratio >1) while 63 were enriched in the U1 precipitate (Lhx1os/U1 ratio<1) (Table S3). A functional association analysis was performed using the online available STRING resource (https://string-db.org/)[49] on the most enriched U1 (Lhx1os/U1 ratio<0.1) and Lhx1os (Lhx1os/U1 ratio>2)

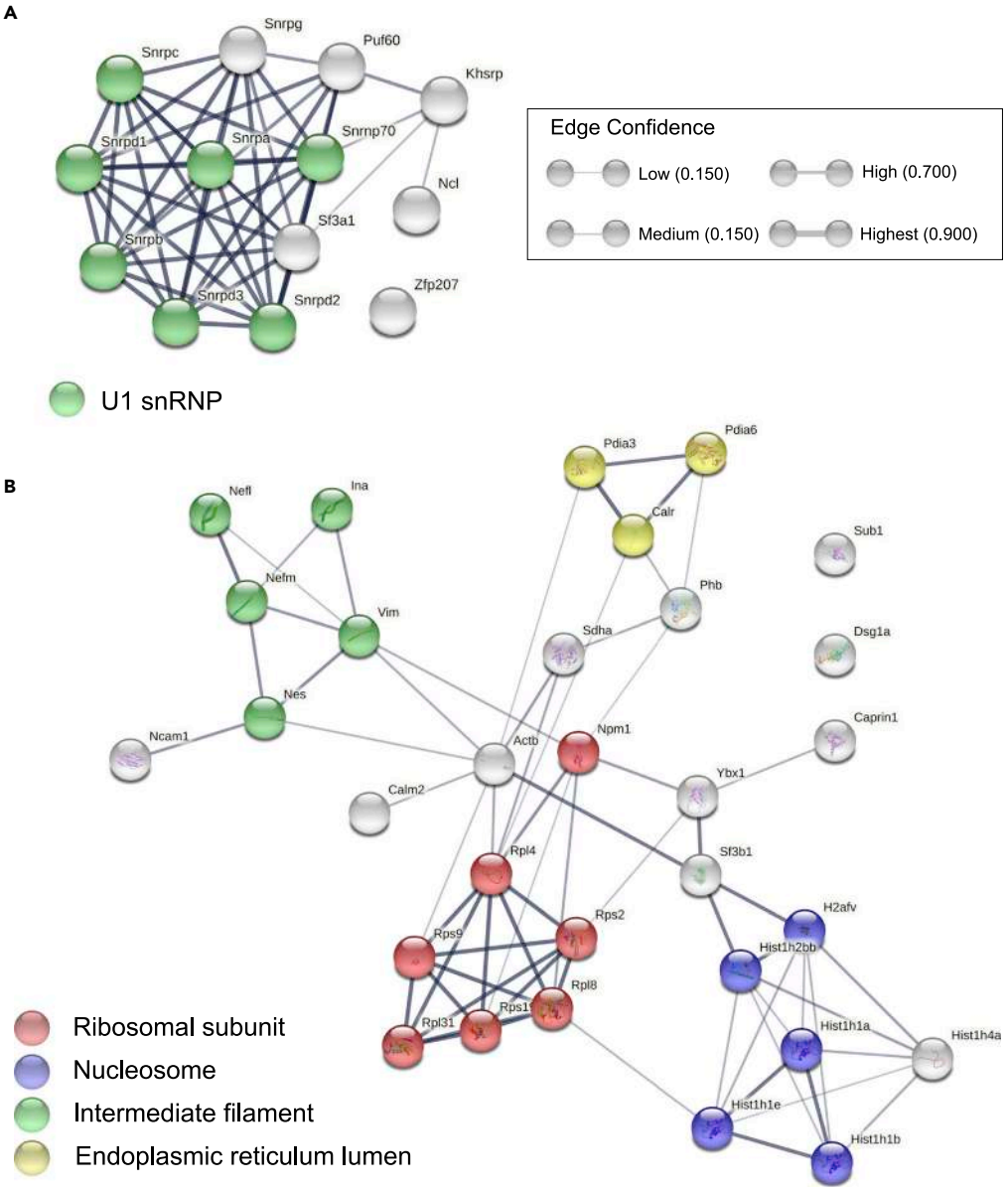

Figure 4. Identification of Lhx1os protein interactors

(A and B) STRING functional network analysis[49] performed on U1 (A) and Lhx1os (B) protein interactors identified by RAP-MS analysis. Different node colors represent the cellular components to which the identified interacting proteins belong ("U1 snRNP" -GO:0005685-, "smooth ER" -GO:0005790-, "intermediate filaments" - GO:0005882-, "nucleosome" -GO:0000786- and "ribosomal subunits" -GO:0044391-). Line thickness between nodes indicates the strength of data support.

interactors. GO term enrichment for the U1 small nuclear RNA identified, as expected, the U1 snRNP proteins as the most enriched in the cellular component category (Figure 4A). The same analysis performed on the Lhx1os RNA identified, in the cellular component category, different GO classes and among them the most represented were those of the smooth ER intermediate filaments, ribosomal subunits, and nucleosomes (Figure 4B).

In vitro validation of Lhx1os and PDIA3 interaction

Since the ER stress pathway was found altered in the KO mice transcriptome and disturbance of the ER proteostasis is recognized as a major driver of neurodegenerative diseases, and in particular of ALS,[50,51] the

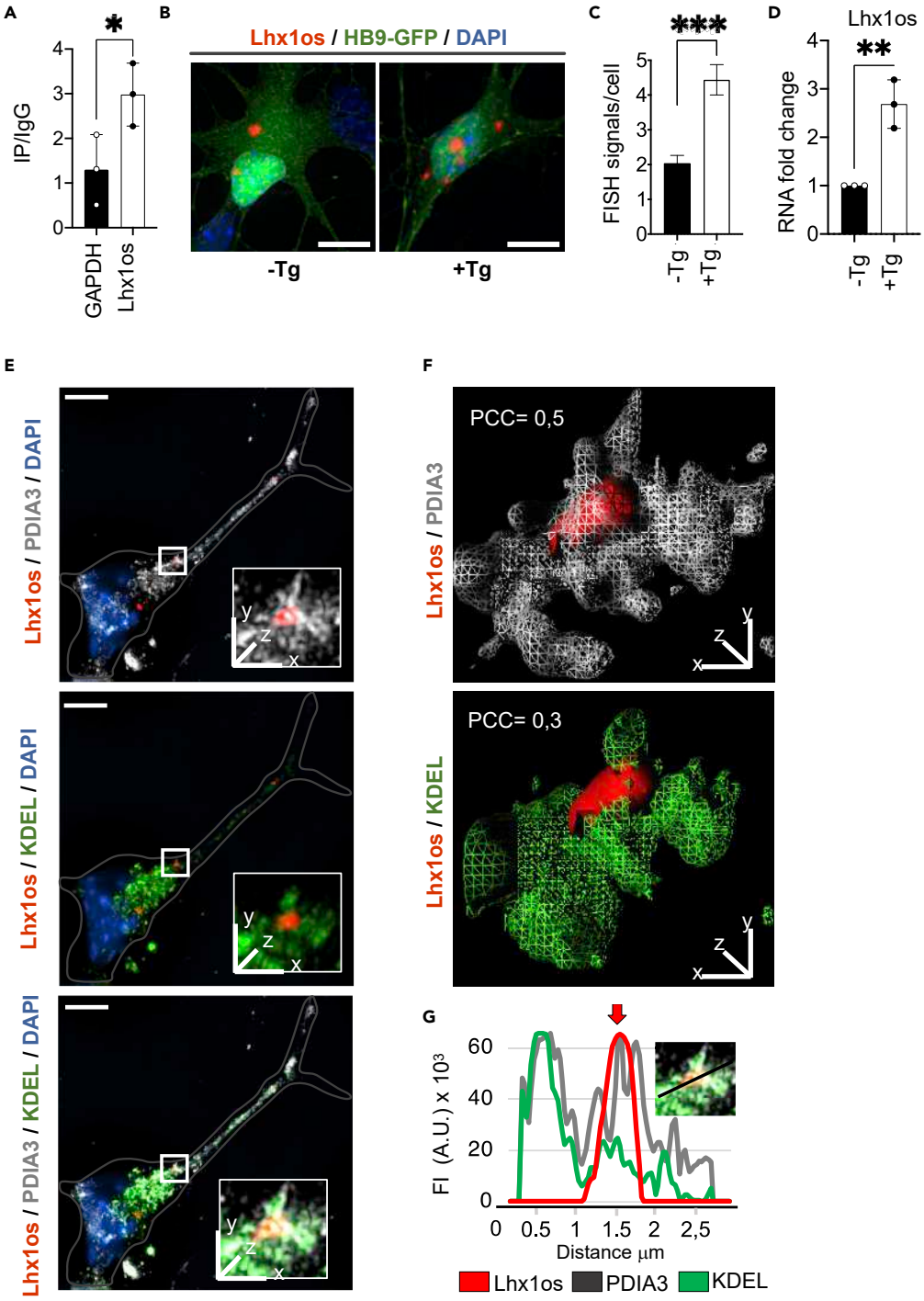

Figure 5. Lhx1os protein interactors analysis

(A) qRT-PCR analysis of Lhx1os enrichment in PDIA3-immunoprecipitate expressed as fold change compared with IgG-immunoprecipitate. Data presented as the mean ± SD of three independent experiments. Statistical analyses were performed using Student *t*-test (*p < 0.05).

(B) Co-staining of Lhx1os RNA (red) and HB9-GFP (green) in mESC-derived MNs untreated (-Tg) or treated (+Tg) for 2 h with the ER stress inducer thapsigargin (Tg). DAPI, 4′,6-diamidino-2-phenylindole. HB9, motor neuron and pancreas homeobox 1. Scale bar = 10 µm.

(C) Quantification of the mean number of spots per MN in cells untreated (-Tg; n = 66) or treated (+Tg; n = 283) with Tg. Data are presented as the mean ± SEM. Statistical analyses were performed using Student *t*-test (***p < 0.001).

Figure 5. *Continued*

(D) qRT-PCR analysis of Lhx1os RNA in mESC-derived MNs exposed to Tg (300 nM) and collected after 4 h of treatment (+Tg) compared to untreated cells (-Tg). The RNA expression levels were normalized against GAPDH mRNA and expressed as relative quantities with respect to untreated cells set to a value of 1. Data are presented as the mean ± SD of three independent experiments. Statistical analyses were performed using Student *t*-test (**$p < 0.01$).

(E) Representative SIM caption performed on mESCs-derived MNs 3 days after dissociation: Basescope™ FISH for Lhx1os (red) and immunofluorescence for PDIA3 (gray) and KDEL (green). The selected region of interest (white square) was enlarged inside the micrographic image. Nucleus was marked with DAPI (blue signal). Scale bar corresponding to 5 μm.

(F) Digital magnification and volume view of region depicted in (E). Pearson's correlation coefficients (PCC) that indicates co-localization index between Lhx1os and PDIA3 or KDEL fluorescence is shown.

(G) Fluorescence intensity (FI) profile of Lhx1os, PDIA3, and KDEL signals, obtained by line-scan method on the region of interest showed in the insert. Fluorescence scanning of single SIM channels is color-coded. Red arrow points the strong overlapping of Lhx1os/PDIA3 fluorescence signals with respect to KDEL profile. The black line in the insert indicates the row of pixel where the intensity values are measured.

PDIA3, PDIA6, and calreticulin (CALR) proteins resulted in interesting candidates. Indeed, they are localized to the smooth ER and participate in the regulation of several ER stress-responsive factors;[52] moreover, PDIA3 and CALR were shown to physically interact.[53]

PDIA3 was selected for further validation of its interaction with Lhx1os. Due to the scarcity of extracts from mESC-differentiated MNs, we analyzed such binding in a reconstituted system where HeLa cells were transfected with expression vectors for Lhx1os and PDIA3. Crosslinking immunoprecipitation (CLIP) experiments using anti-PDIA3 antibodies indicated a significant enrichment of Lhx1os (Figures 5A and S6A). Notably, such enrichment was lost when the UV crosslinking treatment was omitted (Figure S6B). The overexpression of an unrelated lncRNA[54] was used as IP-negative control (Figure S6B, right panel).

To further validate this interaction, we proceeded with *in situ* analysis. Preliminarily, we explored the subcellular localization of Lhx1os lncRNA by RNA fluorescence *in situ* hybridization (FISH) in mESC-derived MNs. Lhx1os detection was performed by using the BaseScope™ assay,[55,56] with a probe set targeting two exon junctions shared among the major Lhx1os isoforms. The results indicate that Lhx1os has a punctate distribution mainly in the cytoplasm (Figure 5B, left panel and S6C-D), confirming the molecular analysis conducted by Biscarini et al. (2018),[28] in which it was shown that approximately 80% of the Lhx1os transcript has cytoplasmic localization in contrast with the 20% nuclear localization. Interestingly, when MNs were treated with thapsigargin (Tg), a commonly used ER stressor,[57] the number of FISH spots increased (Figures 5B, 5C, and S6E), indicating that Lhx1os expression itself is under the control of the ER stress response. Such increase was also confirmed by the RNA levels measured by qRT-PCR (Figure 5D). The upregulation of Herpud1 expression was verified by qPCR and used as a positive control of the ER stress induction upon Tg treatment[46] (Figure S6F). Moreover, the upregulation observed after Tg administration was lost upon actinomycin D treatment, indicating that Lhx1os upregulation is due to its transcriptional activation and not to an increase in RNA stability (Figure S6G).

FISH was then combined with PDIA3 or KDEL (a canonical motif shared among several ER-associated proteins) immunofluorescence. The use of these two antibodies allows us to distinguish the PDIA3 signals since this protein has a C-terminal QEDL ER retention signal different from the canonical KDEL domain present, among the others, in the CALR and PDIA6 proteins.[58] The results indicate that Lhx1os co-localizes with the two ER-specific markers (representative images are shown in Figures 5E and S7A). The 3D rendering combined with Pearson's correlation quantification showed that while the KDEL signals are in proximity of Lhx1os, those visualized with PDIA3 antibodies exhibit quite an intimate association with the lncRNA, indicating a major degree of spatial association of Lhx1os with PDIA3 with respect to KDEL-containing proteins (representative images are shown in Figures 5F, S7B, S7D, and Videos S1 and S2).

Moreover, the overlap occurrence of Lhx1os signals and ER markers was tested by linescan analysis, which depicts the fluorescence intensity along a linear segment in the images. In this assay, Lhx1os RNA (red) shows a preferential overlapping with PDIA3 (gray) peaks than with the KDEL (green) ones (Figures 5G, S7C, and S7E). These results indicate that the Lhx1os RNA is localized at the level of the ER compartment, where it is in intimate connection with the PDIA3 protein.

Interestingly, the same degree of spatial association between Lhx1os and PDIA3 was maintained upon thapsigargin treatment (representative images are shown in Figure S8A), as also indicated by the Pearson's correlation quantification (Figure S8B).

Altogether, the biochemical and imaging data demonstrate that Lhx1os and PDIA3 are in complex inside the cell and in proximity with KDEL containing proteins; it is possible that among them there could be CALR and PDIA6, both identified in RAP experiments. Moreover, Lhx1os is upregulated upon ER stress, similarly to most of the protein factors commonly involved in UPR.

Lhx1os and PDIA3 control the same ER stress-response factors

The physical interaction of Lhx1os and PDIA3, together with the altered expression of genes regulating the ER stress response found in the spinal cords of Lhx1os KO mice (Figure 3C), pointed to their possible combined activity on the UPR to protect cells from ER stress.

Therefore, we tested in an *in vitro* cellular system whether Lhx1os can be modulated by the ER stress response and whether its downregulation impinges on the same pathway identified *in vivo*. Interestingly, we found that Lhx1os expression is also upregulated upon treatment of murine N2a neuroblastoma cells with thapsigargin, similarly to what was found in mESC-derived MNs (compare Figure 6A with Figure 5D). Also, the expression of PDIA3 mRNA was induced upon stress (Figure 6A). In the same experiment, we could observe the upregulation of several ER stress-response genes such as those found deregulated in the KO mice (compare Figure 6A with Figure 3C), indicating that the overall response to the ER stress can be appropriately reproduced in this cellular system. N2a cells were then treated with scramble siRNAs (siSCR) and siRNAs against Lhx1os (siLhx1os) in the presence or absence of thapsigargin. Figure 6B shows that, upon Lhx1os downregulation, the expression of the same ER stress marker genes affected in the KO mice is significantly decreased in N2a cells and that this effect is more consistent in the presence of Tg. Notably, PDIA3 levels were not affected, confirming data of the *in vivo* transcriptome, and pointing out that PDIA3 expression is independent from the Lhx1os levels (Figure 6B). Rescue experiments were performed in N2a cells using a depleted form of Lhx1os resistant to siRNAs (Lhx1osΔsi). N2a cells were treated with siSCR and siLhx1os in the presence of an empty plasmid (ctrl) or a plasmid overexpressing Lhx1osΔsi (Lhx1osΔsi). As shown in Figure S9, the effects of the downregulation of Lhx1os on the target genes were rescued by the overexpression of the Lhx1osΔsi.

These results demonstrate that the depletion of Lhx1os in N2a cells faithfully recapitulates the molecular phenotype observed *in vivo*; furthermore, they confirm that these effects are due to the overall levels of Lhx1os and not to any peculiar alternative spliced isoform, allowing to exclude the possibility that the observed *in vivo* phenotype could be due to a dominant-negative effect of the residual alternative-spliced Lhx1os isoform (Lhx1os-Δex2) observed in KO animals.

Furthermore, the depletion of PDIA3 affected the expression of the same set of genes, even if the effect was significant only under stress conditions (Figure 6B). Altogether, these results indicate that both Lhx1os and PDIA3 impinge on the same pathway which includes genes upregulated upon the ER stress response, while they do not control their reciprocal synthesis.

DISCUSSION

In this work we raised a mouse model to study the *in vivo* function of a lncRNA and found several features that link its role to MN function and homeostasis. Although the analysis of Lhx1os expression in different tissues showed its presence also in other districts of the CNS (e.g., hypothalamus and cerebellum) as well as in the kidney, we focused on its function in the spinal cord due to its enriched expression in both mouse and human MNs. Moreover, its expression was shown to increase in MNs with genetic backgrounds associated with ALS.[28] We show that Lhx1os KO animals display a phenotype which recapitulates several aspects of MN malfunctioning, such as MN reduction and motor impairment, providing an interesting case where a mammalian lncRNA concurs in such control. Altogether, these data allow us to suggest a possible link between the lack of Lhx1os and MN disorders.

Interestingly, the motor dysfunctions observed in KO mice were comparable to those observed in several ALS animal model systems with mutations in ALS-associated proteins.[59–64] Indeed, already at 3 months of age (P90), we observed impairment in both the hanging steel and the treadmill tests. These performances further worsened in 6-month-old animals (P180).

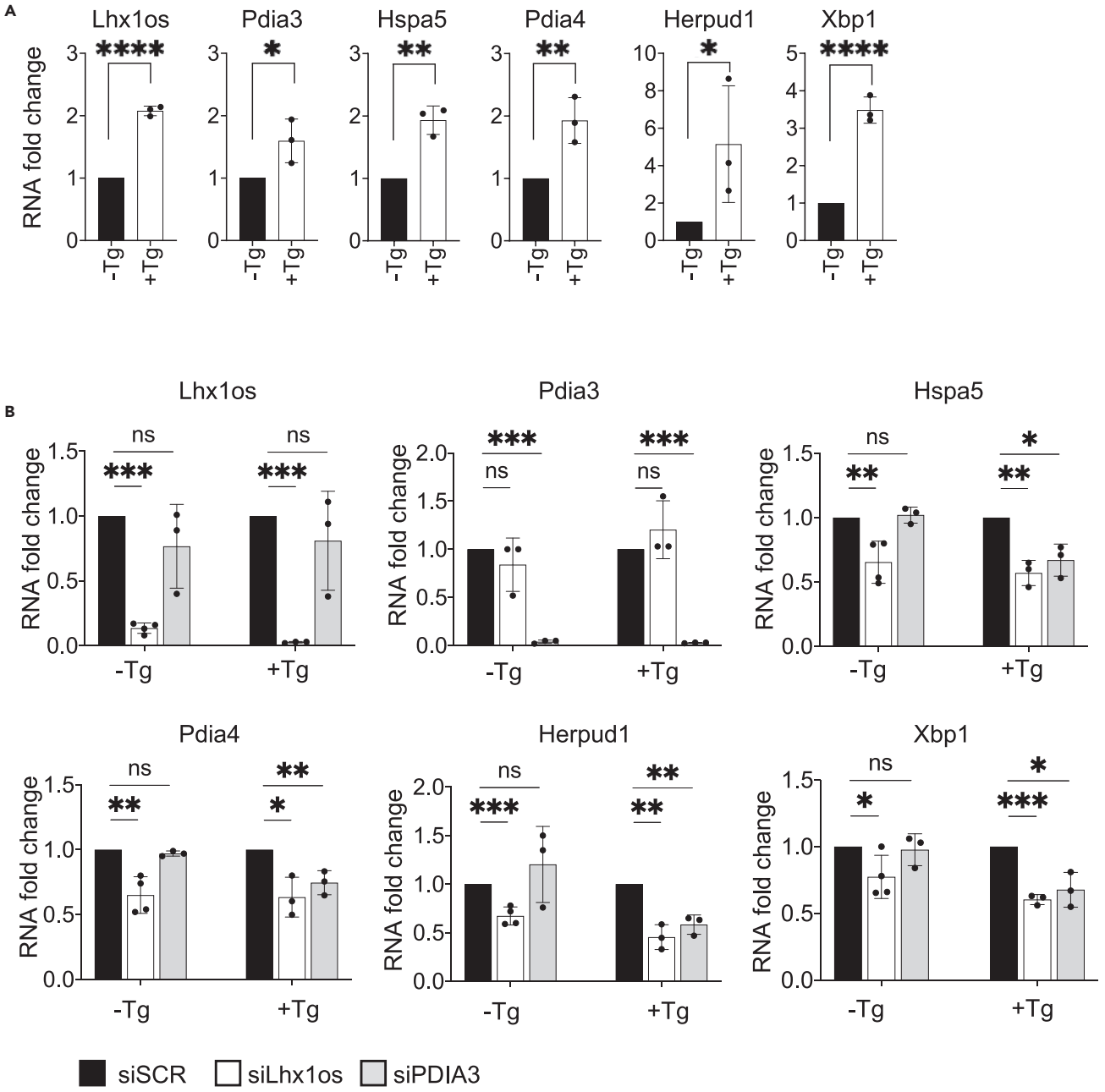

Figure 6. Effects of Lhx1os and Pdia3 *in vitro* depletion in N2a cells

(A) qRT-PCR analysis of the indicated RNAs in N2a cells exposed to Tg (500 nM) and collected after 2 h of treatment (+Tg) compared to untreated cells (-Tg). The RNA expression levels were normalized against GAPDH mRNA and expressed as relative quantities with respect to untreated cells set to a value of 1. Data are presented as the mean ± SD of 3 independent experiments. Statistical analyses were performed using Student *t*-test (*p < 0.05, **p < 0.01, ****p < 0.0001).

(B) qRT-PCR analysis of the indicated RNAs in N2a cells treated with scramble siRNAs (siScr) and siRNAs against Lhx1os (siLhx1os) or Pdia3 (siPdia3) and exposed (+Tg) or not (-Tg) to thapsigargin (500 mM) for 2 h. The RNA expression levels were normalized against GAPDH mRNA and expressed as relative quantities with respect to siScr-treated cells set to a value of 1. Data are presented as the mean ± SD of at least 3 independent experiments. Statistical analyses were performed using Student *t*-test (ns p>0.05, *p < 0.05, **p < 0.01, ***p < 0.001).

In addition to the functional tests, also morphological studies supported Lhx1os involvement in MN homeostasis. In fact, while the count of MNs in the coronal sections of WT lumbar SCs showed no variation among the different stages analyzed (P7, P90, and P180), the number of MNs in Lhx1os KO SCs decreased between P7

and P90 and remained constant until 6 months of age (P180). Since no differences between WT and KO mice were observed at P7, we could conclude that the absence of Lhx1os does not affect MN development during embryogenesis, but that instead it causes specific postnatal effects. The first is represented by a decrease in the number of large MNs (diameter >20 μm) that reached a plateau after the initial three months of life (P90). It is known that during the first three weeks of a mouse's life not only motor circuits but also MNs continue to mature.[41] Moreover, the spinal MN pools are composed by alfa and gamma motor neurons that derive from common progenitors[65] and the morphological discrimination between the two types is primarily based on their size, being the diameter of gamma MNs normally smaller than that of alfa MNs.[38] However, this dimensional aspect becomes evident only when mice reach maturity, while during early postnatal development the difference in size is small and not sufficient to distinguish one type of MN from the other.[41] In this paper, double-positive cells for Nissl and ChAT staining from postnatal mice SC (P7) were considered as MNs, independently of their dimensions; in SC sections from mature mice (P90 and P180), also a diameter value > 20 μm, based on commonly accepted MN count protocols,[37–40] was considered.

Downstream of these considerations, we cannot rule out the possibility that in Lhx1os KO mice, the decrease in large MNs could be due to specific defects in alfa MN maturation.

The second observed postnatal event is reflected by the worsening of the motor performance, observed between P90 and P180, despite further lack of MNs. This can be explained by the impairment in MN function during advancing age, according to the observation that the loss of synaptic inputs in older animals leads to deterioration of motor function without reduction in MN number.[66,67] We cannot exclude that such explanation might also be valid for the Lshx1os KO animals.

In this paper, we also provide evidence for the mechanism of Lhx1os action that impinge on the ER stress response and on the UPR, important cellular pathways recognized as major drivers of neurodegenerative processes.

The UPR is an adaptive response to ER stress based on strictly interconnected signaling pathways that are mediated by three specific ER stress *trans*-membrane sensors: the kinase/endoribonuclease inositol-requiring protein-1 (IRE1α), the activating transcription factor 6 (ATF6), and the protein kinase RNA-like ER kinase.[68] Triggering of these pathways can be mediated by misfolded protein accumulation as well as by alterations in the ionic balance of the cell (e.g., perturbation of calcium homeostasis). As a consequence of this activation, protein-folding enzymes and chaperones are upregulated to counteract unfolded protein accumulation; in turn, the degradation of misfolded proteins is enhanced and protein translation is reduced.[68]

Interestingly, we found that several Lhx1os interactors correspond to proteins associated with the ER; among them, calreticulin, calnexin, and PDIA3 are known to transiently bind newly synthesized glycoproteins in the ER.[52] We were able to validate PDIA3, a member of the family of protein disulfide isomerases (PDIs) which controls protein folding through their ability to form and break disulfide bonds,[69] as a bona fide Lhx1os interactor. Notably, we show that the downregulation of either Lhx1os or PDIA3 affects the same set of ER stress-response genes, indicating that both components impinge on the same regulatory pathway. Moreover, the almost complete depletion of Lhx1os in cells was achieved using siRNAs, thus avoiding the production of the Lhx1os-ΔEx2 form observed in mice. These results demonstrated that the identified targets respond to the decrease of Lhx1os levels and that the ΔEx2 isoform produced in mice was not responsible for those changes.

Under ER stress conditions, Hspa5, the key repressor of the UPR pathway, disassociates from the three specific ER stress *trans*-membrane sensors, causing several downstream events and, among the others, the nuclear translocation of ATF6 where it activates the ER chaperone genes involved in the UPR.[70] ATF6 activation was described to rely also on the activity of PDIA5, an ER-associated protein.[71] In our system, we show that PDIA3 controls the same downstream pathway as PDIA5 and, more intriguingly, that it elicits its activity in cooperation with the MN-enriched RNA Lhx1os. Whether PDIA3 has a redundant function with respect to PDIA5, or whether this is a peculiarity of the specific cellular system analyzed, has still to be investigated.

Interestingly, the UPR is associated with diverse pathological conditions and is strongly activated in neurodegenerative disorders.[43,72,73]

The molecular mechanism that we have identified could be linked with the ALS pathology since disturbance of the ER proteostasis is recognized as a major driver of neurodegenerative diseases and it is also indicated as a common feature of sporadic and familial forms of ALS.[51,74] Moreover, in ALS, the UPR is activated to return ER to its normal physiological activity and for the recovery of MN homeostasis. Notably, four ALS-linked mutations were recently identified in two major PDI genes, PDIA1 and PDIA3.[50]

Finally, also Lhx1os shows a link with the ALS pathology; in fact, it is upregulated in mouse MNs carrying mutations in the ALS-associated FUS protein.[28] Since we show that Lhx1os contributes to positively regulate the ER stress response, we suggest that its increase in MNs carrying ALS-associated mutations could represent an adaptive response to aberrant protein expression.

We also propose that the conserved Lhx1os human counterpart could be an interesting candidate for the identification of novel mutations causing MN-associated diseases in human.

Limitations of the study

One of the limits of this study is the methodology utilized to reveal the subcellular localization of Lhx1os transcript that does not allow to assess how widespread is the localization of Lhx1os molecules on the ER and their abundance. This is likely due to limits of the Basescope technology (Advanced Cell Diagnostics) itself which, being based on exponential enzymatic signal amplification, can lead to the uneven visualization and quantification of the lncRNA molecules in the different subcellular compartments. Moreover, the proteinase treatment, needed to increase the target sequence accessibility, could differentially make available RNA molecules for probes interaction.

A second limitation is represented by the fact that only male mice were used for the functional tests. In the treadmill task which lasts 15 days, the female estrus cycle phases would have affected behavioral performance differently,[75] thus requiring the use of larger number of animals. Moreover, also body weight differences between females and males would have required independent analyses doubling the number of mice. The choice of using only males then complies with the three R principles required in animal experimentation.

STAR★METHODS

Detailed methods are provided in the online version of this paper and include the following:

- KEY RESOURCES TABLE
- RESOURCE AVAILABILITY
  - Lead contact
  - Materials availability
  - Data and code availability
- EXPERIMENTAL MODEL AND SUBJECT DETAILS
  - Generation of mouse line
  - Cell cultures conditions and treatments
- METHOD DETAILS
  - Lhx1os 5′RACE PCR
  - Behavioral and functional tests
  - Open field test
  - Hanging steel test
  - Treadmill exhaustion test
  - Motor neuron count
  - RNA-FISH and immunofluorescence
  - Mouse tissue collection for molecular analysis
  - RNA extraction and quantification by qRT-PCR
  - Protein extraction and western blot
  - Overexpression constructs
  - RNA antisense purification-mass spectrometry (RAP-MS) assay
  - Crosslinking immunoprecipitation (CLIP) assay
  - RNA sequencing
  - Differential expression and gene ontology analyses
- QUANTIFICATION AND STATISTICAL ANALYSIS

SUPPLEMENTAL INFORMATION

Supplemental information can be found online at https://doi.org/10.1016/j.isci.2022.105891.

ACKNOWLEDGMENTS

We would like to thank N. Humphreys and M. Ascolani from the Gene Editing and Embryology Facility (GEEF) at EMBL- Rome for the help in the generation of the mutant mouse line; Dr. P. Bianchini and Dr. M. Oneto (Nanoscopy and NIC@IIT, Istituto Italiano di Tecnologia, Genoa, Italy) for providing N-SIM microscope and for assistance in image acquisition, and F. Altieri, G. Vicidomini, and A. Diaspro for helpful discussion. We also thank M. Marchioni, M. Arceci, and D. Vozzi for technical help, Dr M. Caruso for assistance and SMART by Servier (https://smart.servier.com/). This work was partially supported by grants from ERC-2019-SyG 855923-ASTRA, Marie Sklodowska-Curie grant agreement N° 721890, AIRC IG 2019 Id. 23053, PRIN 2017 n. 2017P352Z4, H2020 Program "Sapienza Progetti Collaborativi" to I.B., G.T. was supported by MUR 2017ENN4FY to E.D.L.

AUTHOR CONTRIBUTIONS

Conceptualization: J.M. and I.B.; Methodology: J.M. and I.B.; Validation: F.P. and V.P.; Formal analyses: A.S. and S.G.G.; Investigation: F.P., V.P., S.B., T.S., V.S., E.V., D.M., C.M., and G.T.; Data curation: A.S.; Writing-original draft: J.M. and I.B.; Writing-review and editing: J.M., E.D.L., and I.B.; Visualization: F.P., V.P., and A.S.; Supervision: J.M., E.D.L., and I.B.; Funding acquisition: E.D.L. and I.B.

DECLARATION OF INTERESTS

Authors declare that they have no competing interests.

Received: August 31, 2022
Revised: November 22, 2022
Accepted: December 23, 2022
Published: January 20, 2023

REFERENCES

1. Statello, L., Guo, C.-J., Chen, L.-L., and Huarte, M. (2021). Gene regulation by long non-coding RNAs and its biological functions. Nat. Rev. Mol. Cell Biol. *22*, 96–118. https://doi.org/10.1038/s41580-020-00315-9.

2. Ravasi, T., Suzuki, H., Pang, K.C., Katayama, S., Furuno, M., Okunishi, R., Fukuda, S., Ru, K., Frith, M.C., Gongora, M.M., et al. (2006). Experimental validation of the regulated expression of large numbers of non-coding RNAs from the mouse genome. Genome Res. *16*, 11–19. https://doi.org/10.1101/gr.4200206.

3. Derrien, T., Johnson, R., Bussotti, G., Tanzer, A., Djebali, S., Tilgner, H., Guernec, G., Martin, D., Merkel, A., Knowles, D.G., et al. (2012). The GENCODE v7 catalog of human long noncoding RNAs: analysis of their gene structure, evolution, and expression. Genome Res. *22*, 1775–1789. https://doi.org/10.1101/gr.132159.111.

4. Ulitsky, I., and Bartel, D.P. (2013). lincRNAs: genomics, evolution, and mechanisms. Cell *154*, 26–46. https://doi.org/10.1016/j.cell.2013.06.020.

5. Basu, S., Müller, F., and Sanges, R. (2013). Examples of sequence conservation analyses capture a subset of mouse long non-coding RNAs sharing homology with fish conserved genomic elements. BMC Bioinf. *14*, S14. https://doi.org/10.1186/1471-2105-14-S7-S14.

6. Ulitsky, I., Shkumatava, A., Jan, C.H., Sive, H., and Bartel, D.P. (2011). Conserved function of lincRNAs in vertebrate embryonic development despite rapid sequence evolution. Cell *147*, 1537–1550. https://doi.org/10.1016/j.cell.2011.11.055.

7. Diederichs, S. (2014). The four dimensions of noncoding RNA conservation. Trends Genet. *30*, 121–123. https://doi.org/10.1016/j.tig.2014.01.004.

8. Hezroni, H., Koppstein, D., Schwartz, M.G., Avrutin, A., Bartel, D.P., and Ulitsky, I. (2015). Principles of long noncoding RNA evolution derived from direct comparison of transcriptomes in 17 species. Cell Rep. *11*, 1110–1122. https://doi.org/10.1016/j.celrep.2015.04.023.

9. Briggs, J.A., Wolvetang, E.J., Mattick, J.S., Rinn, J.L., and Barry, G. (2015). Mechanisms of long non-coding RNAs in mammalian nervous system development, plasticity, disease, and evolution. Neuron *88*, 861–877. https://doi.org/10.1016/j.neuron.2015.09.045.

10. Ramos, A.D., Andersen, R.E., Liu, S.J., Nowakowski, T.J., Hong, S.J., Gertz, C., Salinas, R.D., Zarabi, H., Kriegstein, A.R., and Lim, D.A. (2015). The long noncoding RNA Pnky regulates neuronal differentiation of embryonic and postnatal neural stem cells. Cell Stem Cell *16*, 439–447. https://doi.org/10.1016/j.stem.2015.02.007.

11. Bond, A.M., Vangompel, M.J.W., Sametsky, E.A., Clark, M.F., Savage, J.C., Disterhoft, J.F., and Kohtz, J.D. (2009). Balanced gene regulation by an embryonic brain ncRNA is critical for adult hippocampal GABA circuitry. Nat. Neurosci. *12*, 1020–1027. https://doi.org/10.1038/nn.2371.

12. Wang, F., Wang, Q., Liu, B., Mei, L., Ma, S., Wang, S., Wang, R., Zhang, Y., Niu, C., Xiong, Z., et al. (2021). The long noncoding RNA Synage regulates synapse stability and neuronal function in the cerebellum. Cell Death Differ. *28*, 2634–2650. https://doi.org/10.1038/s41418-021-00774-3.

13. Riva, P., Ratti, A., and Venturin, M. (2016). The long non-coding RNAs in neurodegenerative diseases: novel mechanisms of pathogenesis. Curr. Alzheimer Res. *13*, 1219–1231. https://doi.org/10.2174/1567205013666160622112234.

14. Zhang, M., He, P., and Bian, Z. (2021). Long noncoding RNAs in neurodegenerative diseases: pathogenesis and potential implications as clinical biomarkers. Front. Mol. Neurosci. *14*, 685143. https://doi.org/10.3389/fnmol.2021.685143.

15. Stifani, N. (2014). Motor neurons and the generation of spinal motor neuron diversity. Front. Cell. Neurosci. *8*, 293. https://doi.org/10.3389/fncel.2014.00293.

16. Vangoor, V.R., Gomes-Duarte, A., and Pasterkamp, R.J. (2021). Long non-coding RNAs in motor neuron development and disease. J. Neurochem. *156*, 777–801. https://doi.org/10.1111/jnc.15198.

17. Chen, K.-W., and Chen, J.-A. (2020). Functional roles of long non-coding RNAs in motor neuron development and disease. J. Biomed. Sci. *27*, 38. https://doi.org/10.1186/s12929-020-00628-z.

18. d'Ydewalle, C., Ramos, D.M., Pyles, N.J., Ng, S.-Y., Gorz, M., Pilato, C.M., Ling, K., Kong, L., Ward, A.J., Rubin, L.L., et al. (2017). The antisense transcript SMN-AS1 regulates SMN expression and is a novel therapeutic target for spinal muscular atrophy. Neuron *93*, 66–79. https://doi.org/10.1016/j.neuron.2016.11.033.

19. Chung, C.-Y., Berson, A., Kennerdell, J.R., Sartoris, A., Unger, T., Porta, S., Kim, H.-J., Smith, E.R., Shilatifard, A., van Deerlin, V., et al. (2018). Aberrant activation of non-coding RNA targets of transcriptional elongation complexes contributes to TDP-43 toxicity. Nat. Commun. *9*, 4406. https://doi.org/10.1038/s41467-018-06543-0.

20. Lo Piccolo, L., and Yamaguchi, M. (2017). RNAi of arcRNA hsrω affects sub-cellular localization of Drosophila FUS to drive neurodiseases. Exp. Neurol. *292*, 125–134. https://doi.org/10.1016/j.expneurol.2017.03.011.

21. Gao, T., Li, J., Li, N., Gao, Y., Yu, L., Zhuang, S., Zhao, Y., and Dong, X. (2020). lncrps25 play an essential role in motor neuron development through controlling the expression of olig2 in zebrafish. J. Cell. Physiol. *235*, 3485–3496. https://doi.org/10.1002/jcp.29237.

22. Yen, Y.P., Hsieh, W.F., Tsai, Y.Y., Lu, Y.L., Liau, E.S., Hsu, H.C., Chen, Y.C., Liu, T.C., Chang, M., Li, J., et al. (2018). Dlk1-Dio3 locus-derived lncRNAs perpetuate postmitotic motor neuron cell fate and subtype identity. Elife *7*, e38080. https://doi.org/10.7554/eLife.38080.

23. Carvelli, A., Setti, A., Desideri, F., Galfrè, S.G., Biscarini, S., Santini, T., Colantoni, A., Peruzzi, G., Marzi, M.J., Capauto, D., et al. (2022). A multifunctional locus controls motor neuron differentiation through short and long noncoding RNAs. EMBO J. *41*, e108918. https://doi.org/10.15252/embj.2021108918.

24. Nishimoto, Y., Nakagawa, S., Hirose, T., Okano, H.J., Takao, M., Shibata, S., Suyama, S., Kuwako, K.-I., Imai, T., Murayama, S., et al. (2013). The long non-coding RNA nuclear-enriched abundant transcript 1_2 induces paraspeckle formation in the motor neuron during the early phase of amyotrophic lateral sclerosis. Mol. Brain *6*, 31. https://doi.org/10.1186/1756-6606-6-31.

25. Mizielinska, S., Grönke, S., Niccoli, T., Ridler, C.E., Clayton, E.L., Devoy, A., Moens, T., Norona, F.E., Woollacott, I.O.C., Pietrzyk, J., et al. (2014). C9orf72 repeat expansions cause neurodegeneration in Drosophila through arginine-rich proteins. Science *345*, 1192–1194. https://doi.org/10.1126/science.1256800.

26. Li, P.P., Sun, X., Xia, G., Arbez, N., Paul, S., Zhu, S., Peng, H.B., Ross, C.A., Koeppen, A.H., Margolis, R.L., et al. (2016). ATXN2-AS, a gene antisense to ATXN2, is associated with spinocerebellar ataxia type 2 and amyotrophic lateral sclerosis. Ann. Neurol. *80*, 600–615. https://doi.org/10.1002/ana.24761.

27. Gagliardi, S., Zucca, S., Pandini, C., Diamanti, L., Bordoni, M., Sproviero, D., Arigoni, M., Olivero, M., Pansarasa, O., Ceroni, M., et al. (2018). Long non-coding and coding RNAs characterization in peripheral blood mononuclear cells and spinal cord from amyotrophic lateral sclerosis patients. Sci. Rep. *8*, 2378. https://doi.org/10.1038/s41598-018-20679-5.

28. Biscarini, S., Capauto, D., Peruzzi, G., Lu, L., Colantoni, A., Santini, T., Shneider, N.A., Caffarelli, E., Laneve, P., and Bozzoni, I. (2018). Characterization of the lncRNA transcriptome in mESC-derived motor neurons: implications for FUS-ALS. Stem Cell Res. *27*, 172–179. https://doi.org/10.1016/j.scr.2018.01.037.

29. Ip, C.K., Fossat, N., Jones, V., Lamonerie, T., Tam, P.P.L., Ip, C.K., Fossat, N., and Tam, P.P.L. (2014). Head formation: otx2 regulates dkk1 and lhx1 activity in the anterior mesendoderm. Development (Camb.) *141*, 3859–3867. https://doi.org/10.1242/dev.114900.

30. Fossat, N., Ip, C.K., Jones, V.J., Studdert, J.B., Khoo, P.L., Lewis, S.L., Power, M., Tourle, K., Loebel, D.A.F., Kwan, K.M., et al. (2015). Context-specific function of the LIM homeobox 1 transcription factor in head formation of the mouse embryo. Development (Camb.) *142*, 2069–2079. https://doi.org/10.1242/dev.120907.

31. Costello, I., Nowotschin, S., Sun, X., Mould, A.W., Hadjantonakis, A.-K., Bikoff, E.K., and Robertson, E.J. (2015). Lhx1 functions together with Otx2, Foxa2, and Ldb1 to govern anterior mesendoderm, node, and midline development. Genes Dev. *29*, 2108–2122. https://doi.org/10.1101/gad.268979.

32. Barnes, J.D., Crosby, J.L., Jones, C.M., Wright, C.V., and Hogan, B.L. (1994). Embryonic expression of lim-1, the mouse homolog of Xenopus XLim-1, suggests a role in lateral mesoderm differentiation and neurogenesis. Dev. Biol. *161*, 168–178.

33. Abugessaisa, I., Noguchi, S., Hasegawa, A., Kondo, A., Kawaji, H., Carninci, P., and Kasukawa, T. (2019). refTSS: a reference data set for human and mouse transcription start sites. J. Mol. Biol. *431*, 2407–2422. https://doi.org/10.1016/j.jmb.2019.04.045.

34. FANTOM Consortium and the RIKEN PMI and CLST DGT, Forrest, A.R.R., Kawaji, H., Rehli, M., Baillie, J.K., de Hoon, M.J.L., Haberle, V., Lassmann, T., Kulakovskiy, I.V., Lizio, M., et al. (2014). A promoter-level mammalian expression atlas. Nature *507*, 462–470. https://doi.org/10.1038/nature13182.

35. Luo, S., Lu, J.Y., Liu, L., Yin, Y., Chen, C., Han, X., Wu, B., Xu, R., Liu, W., Yan, P., et al. (2016). Divergent lncRNAs regulate gene expression and lineage differentiation in pluripotent cells. Cell Stem Cell *18*, 637–652. https://doi.org/10.1016/j.stem.2016.01.024.

36. Castro, B., and Kuang, S. (2017). Evaluation of muscle performance in mice by treadmill exhaustion test and whole-limb grip strength assay. Bio. Protoc. *7*, e2237. https://doi.org/10.21769/BioProtoc.2237.

37. Ferrucci, M., Lazzeri, G., Flaibani, M., Biagioni, F., Cantini, F., Madonna, M., Bucci, D., Limanaqi, F., Soldani, P., and Fornai, F. (2018). In search for a gold-standard procedure to count motor neurons in the spinal cord. Histol. Histopathol. *33*, 1021–1046. https://doi.org/10.14670/HH-11-983.

38. Friese, A., Kaltschmidt, J.A., Ladle, D.R., Sigrist, M., Jessell, T.M., and Arber, S. (2009). Gamma and alpha motor neurons distinguished by expression of transcription factor Err3. Proc. Natl. Acad. Sci. USA *106*, 13588–13593. https://doi.org/10.1073/pnas.0906809106.

39. Avossa, D., Grandolfo, M., Mazzarol, F., Zatta, M., and Ballerini, L. (2006). Early signs of motoneuron vulnerability in a disease model system: characterization of transverse slice cultures of spinal cord isolated from embryonic ALS mice. Neuroscience *138*, 1179–1194. https://doi.org/10.1016/j.neuroscience.2005.12.009.

40. Riancho, J., Ruiz-Soto, M., Villagrá, N.T., Berciano, J., Berciano, M.T., and Lafarga, M. (2014). Compensatory motor neuron response to chromatolysi in the murine hSOD1G93A model of amyotrophic lateral sclerosis. Front. Cell. Neurosci. *8*, 346. https://doi.org/10.3389/fncel.2014.00346.

41. Shneider, N.A., Brown, M.N., Smith, C.A., Pickel, J., and Alvarez, F.J. (2009). Gamma motor neurons express distinct genetic markers at birth and require muscle spindle-derived GDNF for postnatal survival. Neural Dev. *4*, 42. https://doi.org/10.1186/1749-8104-4-42.

42. Lance-Jones, C. (1982). Motoneuron cell death in the developing lumbar spinal cord of the mouse. Brain Res. *256*, 473–479. https://doi.org/10.1016/0165-3806(82)90192-4.

43. Montibeller, L., and de Belleroche, J. (2018). Amyotrophic lateral sclerosis (ALS) and Alzheimer's disease (AD) are characterised by differential activation of ER stress pathways: focus on UPR target genes. Cell Stress Chaperones *23*, 897–912. https://doi.org/10.1007/s12192-018-0897-y.

44. Wang, J., Lee, J., Liem, D., and Ping, P. (2017). HSPA5 Gene encoding Hsp70 chaperone BiP in the endoplasmic reticulum. Gene *618*, 14–23. https://doi.org/10.1016/j.gene.2017.03.005.

45. Yoshida, H., Matsui, T., Yamamoto, A., Okada, T., and Mori, K. (2001). XBP1 mRNA Is Induced by ATF6 and Spliced by IRE1 in Response to ER Stress to Produce a Highly Active Transcription Factor phorylation, the activated Ire1p specifically cleaves HAC1 precursor mRNA to remove an intron of 252 nucle-otides. The cleaved 5 and 3 halves of mature HAC1 mRNA are ligated by Rlg1p

(tRNA ligase). HAC1 mRNA Encodes the Basic Leucine Zipper (bZIP).

46. Hori, O., Ichinoda, F., Yamaguchi, A., Tamatani, T., Taniguchi, M., Koyama, Y., Katayama, T., Tohyama, M., Stern, D.M., Ozawa, K., et al. (2004). Role of Herp in the endoplasmic reticulum stress response. Gene Cell. *9*, 457–469. https://doi.org/10.1111/j.1356-9597.2004.00735.x.

47. Chan, S.L., Fu, W., Zhang, P., Cheng, A., Lee, J., Kokame, K., and Mattson, M.P. (2004). Herp stabilizes neuronal Ca2+ homeostasis and mitochondrial function during endoplasmic reticulum stress. J. Biol. Chem. *279*, 28733–28743. https://doi.org/10.1074/jbc.M404272200.

48. McHugh, C.A., and Guttman, M. (2018). RAP-MS: a method to identify proteins that interact directly with a specific RNA molecule in cells. Methods Mol Biol. *1649*, 473–488. https://doi.org/10.1007/978-1-4939-7213-5_31.

49. Szklarczyk, D., Gable, A.L., Lyon, D., Junge, A., Wyder, S., Huerta-Cepas, J., Simonovic, M., Doncheva, N.T., Morris, J.H., Bork, P., et al. (2019). STRING v11: protein-protein association networks with increased coverage, supporting functional discovery in genome-wide experimental datasets. Nucleic Acids Res. *47*, D607–D613. https://doi.org/10.1093/nar/gky1131.

50. Woehlbier, U., Colombo, A., Saaranen, M.J., Pérez, V., Ojeda, J., Bustos, F.J., Andreu, C.I., Torres, M., Valenzuela, V., Medinas, D.B., et al. (2016). ALS -linked protein disulfide isomerase variants cause motor dysfunction. EMBO J. *35*, 845–865. https://doi.org/10.15252/embj.201592224.

51. Roussel, B.D., Kruppa, A.J., Miranda, E., Crowther, D.C., Lomas, D.A., and Marciniak, S.J. (2013). Endoplasmic reticulum dysfunction in neurological disease. Lancet Neurol. *12*, 105–118. https://doi.org/10.1016/S1474-4422.

52. Ellgaard, L., and Frickel, E.M. (2003). Calnexin, calreticulin, adn ERp57. Cell Biochem. Biophys. *39*, 223–247. https://doi.org/10.1385/CBB.

53. Leach, M.R., Cohen-Doyle, M.F., Thomas, D.Y., and Williams, D.B. (2002). Localization of the lectin, ERp57 binding, and polypeptide binding sites of calnexin and calreticulin. J. Biol. Chem. *277*, 29686–29697. https://doi.org/10.1074/jbc.M202405200.

54. Martone, J., Mariani, D., Santini, T., Setti, A., Shamloo, S., Colantoni, A., Capparelli, F., Paiardini, A., Dimartino, D., Morlando, M., and Bozzoni, I. (2020). SMaRT lncRNA controls translation of a G-quadruplex-containing mRNA antagonizing the DHX36 helicase. EMBO Rep. *21*, e49942. https://doi.org/10.15252/embr.201949942.

55. Rossi, F., Legnini, I., Megiorni, F., Colantoni, A., Santini, T., Morlando, M., di Timoteo, G., Dattilo, D., Dominici, C., and Bozzoni, I. (2019). Circ-ZNF609 regulates G1-S progression in rhabdomyosarcoma. Oncogene *38*, 3843–3854. https://doi.org/10.1038/s41388-019-0699-4.

56. D'Ambra, E., Santini, T., Vitiello, E., D'Uva, S., Silenzi, V., Morlando, M., and Bozzoni, I. (2021). Circ-Hdgfrp3 shuttles along neurites and is trapped in aggregates formed by ALS-associated mutant FUS. iScience *24*, 103504. https://doi.org/10.1016/j.isci.2021.103504.

57. Kaufman, R.J. (1999). Stress signaling from the lumen of the endoplasmic reticulum: coordination of gene transcriptional and translational controls. Genes Dev. *13*, 1211–1233. https://doi.org/10.1101/gad.13.10.1211.

58. Wires, E.S., Trychta, K.A., Kennedy, L.M., and Harvey, B.K. (2021). The function of kdel receptors as upr genes in disease. Int. J. Mol. Sci. *22*, 5436. https://doi.org/10.3390/ijms22115436.

59. Huang, S.L., Wu, L.S., Lee, M., Chang, C.W., Cheng, W.C., Fang, Y.S., Chen, Y.R., Cheng, P.L., and Shen, C.K.J. (2020). A robust TDP-43 knock-in mouse model of ALS. Acta Neuropathol. Commun. *8*, 3. https://doi.org/10.1186/s40478-020-0881-5.

60. Iguchi, Y., Katsuno, M., Niwa, J.I., Takagi, S., Ishigaki, S., Ikenaka, K., Kawai, K., Watanabe, H., Yamanaka, K., Takahashi, R., et al. (2013). Loss of TDP-43 causes age-dependent progressive motor neuron degeneration. Brain *136*, 1371–1382. https://doi.org/10.1093/brain/awt029.

61. Sharma, A., Lyashchenko, A.K., Lu, L., Nasrabady, S.E., Elmaleh, M., Mendelsohn, M., Nemes, A., Tapia, J.C., Mentis, G.Z., and Shneider, N.A. (2016). ALS-associated mutant FUS induces selective motor neuron degeneration through toxic gain of function. Nat. Commun. *7*, 10465. https://doi.org/10.1038/ncomms10465.

62. Shelkovnikova, T.A., Peters, O.M., Deykin, A.v., Connor-Robson, N., Robinson, H., Ustyugov, A.A., Bachurin, S.O., Ermolkevich, T.G., Goldman, I.L., Sadchikova, E.R., et al. (2013). Fused in sarcoma (FUS) protein lacking nuclear localization signal (NLS) and major RNA binding motifs triggers proteinopathy and severe motor phenotype in transgenic mice. J. Biol. Chem. *288*, 25266–25274. https://doi.org/10.1074/jbc.M113.492017.

63. Philips, T., and Rothstein, J.D. (2015). Rodent models of amyotrophic lateral sclerosis. Curr. Protoc. Pharmacol. *67*, 1–5. https://doi.org/10.1002/0471141755.ph0567s69.

64. Oliván, S., Calvo, A.C., Rando, A., Jesús Muñoz, M., Zaragoza, P., and Osta, R. (2015). Comparative study of behavioural tests in the SOD1G93A mouse model of amyotrophic lateral sclerosis. Exp. Anim. *64*, 147–153. https://doi.org/10.1538/expanim.14-0077.

65. Pfaff, S., and Kintner, C. (1998). Neuronal diversification: development of motor neuron subtypes. Curr. Opin. Neurobiol. *8*, 27–36. https://doi.org/10.1016/s0959-4388(98)80005-6.

66. Chai, R.J., Vukovic, J., Dunlop, S., Grounds, M.D., and Shavlakadze, T. (2011). Striking denervation of neuromuscular junctions without lumbar motoneuron loss in geriatric mouse muscle. PLoS One *6*, e28090. https://doi.org/10.1371/journal.pone.0028090.

67. Maxwell, N., Castro, R.W., Sutherland, N.M., Vaughan, K.L., Szarowicz, M.D., de Cabo, R., Mattison, J.A., and Valdez, G. (2018). α-Motor neurons are spared from aging while their synaptic inputs degenerate in monkeys and mice. Aging Cell *17*, e12726. https://doi.org/10.1111/acel.12726.

68. Hetz, C., Zhang, K., and Kaufman, R.J. (2020). Mechanisms, regulation and functions of the unfolded protein response. Nat. Rev. Mol. Cell Biol. *21*, 421–438. https://doi.org/10.1038/s41580-020-0250-z.

69. Chichiarelli, S., Altieri, F., Paglia, G., Rubini, E., Minacori, M., and Eufemi, M. (2022). ERp57/PDIA3: new insight. Cell. Mol. Biol. Lett. *27*, 12. https://doi.org/10.1186/s11658-022-00315-x.

70. Ye, J., Rawson, R.B., Komuro, R., Chen, X., Davé, U.P., Prywes, R., Brown, M.S., and Goldstein, J.L. (2000). ER stress induces cleavage of membrane-bound ATF6 by the same proteases that process SREBPs. Mol. Cell *6*, 1355–1364. https://doi.org/10.1016/S1097-2765(00)00133-7.

71. Higa, A., Taouji, S., Lhomond, S., Jensen, D., Fernandez-Zapico, M.E., Simpson, J.C., Pasquet, J.-M., Schekman, R., and Chevet, E. (2014). Endoplasmic reticulum stress-activated transcription factor ATF6α requires the disulfide isomerase PDIA5 to modulate chemoresistance. Mol. Cell Biol. *34*, 1839–1849. https://doi.org/10.1128/MCB.01484-13.

72. Hetz, C., Thielen, P., Matus, S., Nassif, M., Court, F., Kiffin, R., Martinez, G., Cuervo, A.M., Brown, R.H., and Glimcher, L.H. (2009). XBP-1 deficiency in the nervous system protects against amyotrophic lateral sclerosis by increasing autophagy. Genes Dev. *23*, 2294–2306. https://doi.org/10.1101/gad.1830709.

73. Ghemrawi, R., and Khair, M. (2020). Endoplasmic reticulum stress and unfolded protein response in neurodegenerative diseases. Int. J. Mol. Sci. *21*, 6127. https://doi.org/10.3390/ijms21176127.

74. Hetz, C., and Mollereau, B. (2014). Disturbance of endoplasmic reticulum proteostasis in neurodegenerative diseases. Nat. Rev. Neurosci. *15*, 233–249. https://doi.org/10.1038/nrn3689.

75. Torromino, G., Maggi, A., and de Leonibus, E. (2021). Estrogen-dependent hippocampal wiring as a risk factor for age-related dementia in women. Prog. Neurobiol. *197*, 101895. https://doi.org/10.1016/j.pneurobio.2020.101895.

76. Montague, T.G., Cruz, J.M., Gagnon, J.A., Church, G.M., and Valen, E. (2014). CHOPCHOP: a CRISPR/Cas9 and TALEN web tool for genome editing. Nucleic Acids Res. *42*, W401–W407. https://doi.org/10.1093/nar/gku410.

77. Wichterle, H., and Peljto, M. (2008). Differentiation of mouse embryonic stem cells to spinal motor neurons. Curr. Protoc. Cell Biol. *5*. https://doi.org/10.1002/9780470151808.sc01h01s5.

78. Errichelli, L., Dini Modigliani, S., Laneve, P., Colantoni, A., Legnini, I., Capauto, D., Rosa, A., de Santis, R., Scarfò, R., Peruzzi, G., et al. (2017). FUS affects circular RNA expression in murine embryonic stem cell-derived motor neurons. Nat. Commun. *8*, 14741. https://doi.org/10.1038/ncomms14741.

79. Guo, J., Qiu, W., Soh, S.L.Y., Wei, S., Radda, G.K., Ong, W.Y., Pang, Z.P., and Han, W. (2013). Motor neuron degeneration in a mouse model of seipinopathy. Cell Death Dis. *4*, e535. https://doi.org/10.1038/cddis.2013.64.

80. Andrews, S. (2010). FastQC: a quality control tool for high throughput sequence data. http://www.bioinformatics.babraham.ac.uk/projects/fastqc/.

81. Saeidipour, B., and Bakhshi, S. (2013). The relationship between organizational culture and knowledge management, & their simultaneous effects on customer relation management. Adv. Environ. Biol. *7*, 2803–2809.

82. Bolger, A.M., Lohse, M., and Usadel, B. (2014). Trimmomatic: a flexible trimmer for Illumina sequence data. Bioinformatics *30*, 2114–2120. https://doi.org/10.1093/bioinformatics/btu170.

83. Dobin, A., Davis, C.A., Schlesinger, F., Drenkow, J., Zaleski, C., Jha, S., Batut, P., Chaisson, M., and Gingeras, T.R. (2013). STAR: ultrafast universal RNA-seq aligner. Bioinformatics *29*, 15–21. https://doi.org/10.1093/bioinformatics/bts635.

84. Anders, S., Pyl, P.T., and Huber, W. (2015). HTSeq-A Python framework to work with high-throughput sequencing data. Bioinformatics *31*, 166–169. https://doi.org/10.1093/bioinformatics/btu638.

85. Love, M.I., Huber, W., and Anders, S. (2014). Moderated estimation of fold change and dispersion for RNA-seq data with DESeq2. Genome Biol. *15*, 550. https://doi.org/10.1186/s13059-014-0550-8.

86. Ignatiadis, N., Klaus, B., Zaugg, J.B., and Huber, W. (2016). Data-driven hypothesis weighting increases detection power in genome-scale multiple testing. Nat. Methods *13*, 577–580. https://doi.org/10.1038/nmeth.3885.

87. Wang, J., Vasaikar, S., Shi, Z., Greer, M., and Zhang, B. (2017). WebGestalt 2017: a more comprehensive, powerful, flexible and interactive gene set enrichment analysis toolkit. Nucleic Acids Res. *45*, W130–W137. https://doi.org/10.1093/nar/gkx356.

STAR★METHODS

KEY RESOURCES TABLE

REAGENT or RESOURCE	SOURCE	IDENTIFIER
Antibodies		
Rabbit polyclonal anti-ERp57 (PDIA3)	Abcam	cat#ab10287; RRID:AB_297026
Rabbit polyclonal anti-LIM1	Thermo Fisher Scientific	cat# PA5-78394; RRID:AB_2736089
Mouse monoclonal anti-GAPDH (6C5)	Santa Cruz Biotechnology	cat# sc-32233; RRID:AB_627679
Mouse monoclonal anti-KDEL	Enzo Life Sciences	cat# SPA-827F; RRID:AB_991595
Goat polyclonal anti-Choline Acetyltransferase (ChAT)	Millipore	cat# AB144P; RRID:AB_2079751
Goat anti-Rabbit IgG (H+L) Secondary Antibody, HRP	Thermo Fisher Scientific	cat# 31460; RRID:AB_228341
Goat anti-Mouse IgG (H+L) Secondary Antibody, HRP	Thermo Fisher Scientific	cat# 32430; RRID:AB_1185566
Goat anti-Rabbit IgG (H+L) Cross-Adsorbed Secondary Antibody, Alexa Fluor 488	ThermoFisher Scientific	cat#A11008; RRID:AB_143165
Donkey anti-Mouse IgG (H+L) Highly Cross-Adsorbed Secondary Antibody, Alexa Fluor Plus 647	ThermoFisher Scientific	cat#A32787; RRID:AB_2762830
Bacterial and virus strains		
Subcloning Efficiency DH5α Competent Cells	Invitrogen	cat#18265-017
MAX Efficiency DH5α Competent Cells	Invitrogen	cat#18258-012
Chemicals, peptides, and recombinant proteins		
Dulbecco's Phosphate Buffered Saline w/o MgCl2 and CaCl2	Sigma-Aldrich	cat#D8537
Dulbecco's Phosphate Buffered Saline with MgCl2 and CaCl2	Sigma-Aldrich	cat#D8662
Trypsin solution from porcine pancreas	Sigma-Aldrich	cat#T4549
Trypsin-EDTA Solution	Sigma-Aldrich	cat#T4299
Trypan blue solution	ThermoFisher Scientific	cat#15250061
EmbryoMax DMEM	Millipore	cat#SLM-220-B
Neurobasal™ Medium	Gibco	cat#21103049
Advanced DMEM/F12	Gibco	cat#12634010
Dulbecco's Modified Eagle's Medium/Nutrient Mixture F-12 Ham	ThermoFisher Scientific	cat#D6421
MEM (Minimum Essential Medium)	Corning	cat#15-010-CV
DMEM- High glucose	Sigma-Aldrich	cat#D6546
Sterile Earle's Balanced Salt Solution (EBSS)	Sigma-Aldrich	cat#E7510
Embryonic stem-cell FBS, qualified, US origin	Gibco	cat#16141-079
KnockOut™ Serum Replacement	ThermoFisher Scientific	cat#10828028
Horse serum	ThermoFisher Scientific	cat#16050122
Fetal Bovine Serum, qualified, Brazil	Gibco	cat#10270-106
Fetal Bovine Serum, qualified, USA	Gibco	cat# LS26140079
Penicillin/Streptomycin	Sigma-Aldrich	cat#P0781

(*Continued on next page*)

Continued

REAGENT or RESOURCE	SOURCE	IDENTIFIER
GlutaMAX™Supplement	ThermoFisher Scientific	cat#35050061
L-glutamine	Sigma-Aldrich	cat#G7513
Sodium Pyruvate	Thermo Fisher Scientific	cat#11360070
MEM non- essential amino acid solution	Sigma-Aldrich	cat#M7145
EmbryoMax non-essential a.a.	Millipore	cat#TMS-001-C
EmbryoMax Nucleosides (100X)	Millipore	cat#ES-008-D
2-mercaptoethanol for ES cells	Millipore	cat#ES-007-E
D-(+)-Glucose solution	Sigma-Aldrich	cat#G8769
B-27™Supplement (50X), serum free	ThermoFisher Scientific	cat#17504001
N-2 supplement	Gibco	cat#17502-001
ESGRO® Recombinant Mouse LIF Protein	Chemicon	cat#ESG11107
GSK-3 Inhibitor XVI	Sigma-Aldrich	cat#361559
PD173074	Sigma-Aldrich	cat#P2499
Smoothened agonist, SAG	Sigma-Aldrich	cat#566660
Retinoic Acid	Sigma-Aldrich	cat#R2625
L-ascorbic acid	Sigma-Aldrich	cat#TMS-001-C
Recombinant Human GDNF	Peprotech	cat#450-44
Recombinant Human CNTF	Peprotech	cat#AF-450-13
Recombinant Human/Murine/Rat BDNF	Peprotech	cat#450-02
Y-27632 dihydrochloride	Sigma-Aldrich	cat#Y0503
Deoxyribonuclease I from bovine pancreas	Sigma-Aldrich	cat#DN25
Papain	Worthington Biochemical Corporation	cat#LK003176
Ovomucoid inhibitor-Albumin	Worthington Biochemical Corporation	cat#LK003182
Poly-L-ornithine	Sigma-Aldrich	cat#P-3655
Murine Laminin	Sigma-Aldrich	cat#L2020
Ultrapure Water with 0.1% Gelatin	Millipore	cat#ES-006-B
Opti-MEM™ Reduced Serum Medium	Thermo Fisher Scientific	cat#31985070
Lipofectamine™ 2000 Transfection Reagent	Thermo Fisher Scientific	cat#11668019
Lipofectamine™ RNAiMAX Transfection Reagent	Thermo Fisher Scientific	cat#13778075
InSolution Thapsigargin	Sigma-Aldrich	cat#67526-95-8
Dimethyl sulfoxide	Sigma-Aldrich	cat#D4540
WesternBright ECL kit	Advansta	cat #K-12045-D20
Mytaq DNA polymerase	Bioline	cat#BIO-21105
CloneAmp™ HiFi PCR Premix	Clontech	cat#639298
FastDigest HindIII	ThermoFisher Scientific	cat#FD0504
FastDigest NotI	ThermoFisher Scientific	cat#FD0594
10X FastDigest Green Buffer	ThermoFisher Scientific	cat#B72
PrimeScript RT Master Mix	TakaraBio	cat#RR036b
Superscript Vilo cDNA Synthesis Kit	Invitrogen	cat#11754050
PowerUp SYBR-Green MasterMix	Thermo Fisher Scientific	cat#4385612
cOmplete™, EDTA-free Protease Inhibitor Cocktail	Roche	cat #11873580001

(*Continued on next page*)

Continued

REAGENT or RESOURCE	SOURCE	IDENTIFIER
NuPAGE 4–12% Bis-Tris Gel	Invitrogen	cat#NP0321
Mini-PROTEAN TGX	Bio-Rad	cat#4568083
Amersham Protran 0.45 µm Nitrocellulose Blotting Membrane	Cytiva	cat#10600002
Difco Skim Milk	BD Life Sciences	cat#232100
4X Laemmli Sample Buffer	Bio-Rad	cat#161-0747
Bio-Rad Protein Assay Dye Reagent Concentrate	Bio-Rad	cat #5000006
Streptavidin MagneSphere Paramagnetic Particles	Promega	cat#Z5481
Dynabeads Protein G	ThermoFisher Scientific	cat#10004D
RNase inhibitors	Thermo Fischer Scientific	cat#EO0384
Proteinase K, recombinant PCR Grade	Roche	cat#03115828001
Tris(2-carboxyethyl)phosphine hydrochloride solution (TCEP)	Sigma-Aldrich	cat#646547
Benzonase nuclease	EMD Millipore	cat#71206
Neurotrace 500/525 Green Fluorescent Nissl stain	Thermo Fisher Scientific	cat# N21480
DAPI for nucleic acid staining	Sigma-Aldrich	cat #D9542
Paraformaldehyde	Electron Microscopy Sciences, Hatfield, PA	cat#15710
Donkey serum	Sigma-Aldrich	cat#D9663
Goat serum	Sigma-Aldrich	cat#G9023
ProLong Diamond Antifade Mountant	Thermo Fisher Scientific	cat#P-36961
Bovin Serum Albumin	Sigma-Aldrich	cat#A9418
Triton X-100	Sigma-Aldrich	cat#9002-93-1
Protease III	ACD	cat#322381
Critical commercial assays		
Direct-Zol RNA MiniPrep Kit	Zymo Research	cat#R2050
miRNeasy Mini Kit	Qiagen	cat#217004
NuceloSpin Gel and PCR Clean-up	MACHEREY-NAGEL	cat#740609.250
Plasmid DNA extraction Mini kit	Fisher Molecular Biology	cat#DE-035
NucleoBond Xtra Midi EF	MACHEREY-NAGEL	cat#740420.50
Genomic DNA Extraction Kit mini	RBC Real Genomics	cat #YGB50
TruSeq Stranded mRNA Library Prep Kit	Illumina	cat #RS-122-2103
NovaSeq 6000 SP Reagent Kit (300 cycles)	Illumina	cat #20027465
FirstChoice® RLM-RACE Kit	Ambion	cat #AM1700
BaseScope Detection Reagent Kit v2	ACD	cat#323910
RNAscope pretreatment reagents	ACD	cat#322381
RNAscope Wash Buffer Reagents	ACD	cat#310091
In-Fusion® HD Cloning Kit	TakaraBio	cat#102518

(*Continued on next page*)

Continued

REAGENT or RESOURCE	SOURCE	IDENTIFIER
Deposited data		
Raw and analyzed data	This paper	GEO: GSE189904
Ensemble (release 99) gene annotation gtf	Ensemble Consortium	http://jan2020.archive.ensembl.org/index.html
Mouse reference genome, GRCm38	Genome Reference Consortium	https://www.ncbi.nlm.nih.gov/assembly/GCF_000001635.20/
Experimental models: Cell lines		
HBG3 ES cell line carrying an Hb9-GFP transgene	Provided by Prof. Niel A. Shneider (Columbia University)	N/A
CF1 Mouse Embryonic Fibroblasts, irradiated	Gibco	cat#A34180
Neuro-2a (N2a)	ATCC	cat#CCL-131
HeLa	ATCC	cat#CCL-2
Experimental models: Organisms/strains		
Mouse C57BL/6J, Lhx1os$^{-/-}$	This paper	N/A
Oligonucleotides		
DNA oligonucleotides used in this work are listed in Table S4	This paper	N/A
siRNAs used in this work are listed in Table S4	This paper	N/A
RAP probe sequences used in this work are listed in Table S4	This paper	N/A
Custom DNA Lhx1os-specific probe for BaseScope™	This paper	cat#703021
Negative control probe for BaseScope™	Rossi et al., 2019[55]	cat#701021
Recombinant DNA		
pcDNA™3.1 (+) Mammalian Expression Vector	Thermo Fisher Scientific	cat#V79020
pcDNA3.1(+) used for cloning mouse Lhx1os	This paper	N/A
pcDNA3.1(+) used for cloning mouse Pdia3	This paper	N/A
Software and algorithms		
ImageLab	Bio-Rad	https://www.bio-rad.com/it-it/product/image-lab-software?ID=KRE6P5E8Z
Prism 9	GraphPad by Dotmatics	https://www.graphpad.com/scientific-software/prism/
QuantStudio 3 and 5 RealTime PCR System Software	Thermo Fisher Scientific	https://www.thermofisher.com/it/en/home/global/forms/life-science/quantstudio-3-5-software.html
MetaMorph Microscopy Automation and Image Analysis Software	Molecular Devices	RRID:SCR_002368 https://www.andImageAnalysis Softwaremoleculardevices.com/products/cellular-imaging-systems/acquisition-and-analysis-software/metamorphmicroscopy#gref

(*Continued on next page*)

Continued

REAGENT or RESOURCE	SOURCE	IDENTIFIER
ImageJ, Fiji distribution	ImageJ	https://imagej.net/software/fiji/downloads
NIS-Elements AR software	Nikon	https://www.microscope.healthcare.nikon.com/en_EU/products/software/nis-elements/nis-elements-advanced-research
FASTQC software	Andrews et al., 2010[80]	https://www.bioinformatics.babraham.ac.uk/projects/fastqc/).
Cutadapt	Saeidipour & Bakhshi, 2013[81]	https://cutadapt.readthedocs.io/en/stable/
Trimmomatic	Bolger et al., 2014[82]	http://www.usadellab.org/cms/?page=trimmomatic
STAR (2.5.2b)	Dobin et al., 2013[83]	https://github.com/alexdobin/STAR
htseq-count software	Anders et al., 2015[84]	https://htseq.readthedocs.io/en/release_0.11.1/count.html
Deseq2 (version 1.30.0)	Love et al., 2014[85]	https://bioconductor.org/packages/release/bioc/html/DESeq2.html
Independent Hypothesis Weighting (IHW version 1.18.0);	Ignatiadis et al., 2016[86]	https://github.com/nignatiadis/IHW
WebGestalt	Wang et al., 2017[87]	http://www.webgestalt.org

RESOURCE AVAILABILITY

Lead contact

Further information and requests for resources and reagents should be directed to and will be fulfilled by the lead contact, Irene Bozzoni (irene.bozzoni@uniroma1.it).

Materials availability

All unique/stable reagents generated in this study are available from the lead contact upon request.

Data and code availability

- The RNA-Seq data from this publication are publicly available at the GEO database with the identifier GEO: GSE189904.
- This paper does not report original code.
- Any additional information required to reanalyze the data reported in this paper is available from the lead contact upon request.

EXPERIMENTAL MODEL AND SUBJECT DETAILS

Generation of mouse line

The mice were housed in the animal facility of EMBL Monterotondo at the Gene Editing and Embryology Facility (GEEF). Mice were maintained in temperature and humidity-controlled condition with food and water provided *ad libitum* and on 12-h light–dark cycle (light on at 7:00).

They were housed in IVC Thoren racks in group of 4 mice/cage. All experiments were approved by the Italian Ministry of health (approval n.82945.56) and conducted within the animal welfare regulations and guidelines. Only males were used for all experiments. Lhx1os knockout mice were generated in the C57BL/6J background using a CRISPR genome-editing system. A single guide RNA, targeting the second exon of Lhx1os, was designed using the https://chopchop.cbu.uib.no/ resource[76] and delivered in fertilized eggs together with an *in vitro* transcribed Cas9 mRNA and a synthetic poly-A site in the form of a 200 nt-long single-stranded donor oligonucleotide (ssODN). ssODN was composed of 100 nt of homology arms and 100 nt of a minimal synthetic poly-A signal, followed by two repetitions of the polymerase destabilizing MAZ sequences. Successful editing was validated by PCR genotyping. gDNA extraction from tail biopsies was performed using RBC Real Genomics DNA Extraction Kit

(RBC Bioscience) according to the manufacturer's protocol. The poly-A/MAZ insertion was detected by PCR, primers are listed in Table S4. A founder F0 male was selected and backcrossed with wild-type mice to generate F1. The Lhx1os KO line was maintained by heterozygous vs heterozygous crosses.

Cell cultures conditions and treatments

All cell lines used in this study were grown at 37°C, 5% CO_2. All cell lines were tested for mycoplasma contamination.

Murine HBG3 ES cells (embryonic stem cells derived from HB9::GFP transgenic mice) were cultured on gelatin-coated or MEF-coated dishes and maintained in mESC medium (Dulbecco's Modified Eagle's Medium for ES, 15% Fetal Bovine Serum for ES, 1X GlutaMAX, 1X Non Essential AmminoAcids, 1X nucleosides, 1X 2-mercaptoethanol and 1X Penicillin/Streptomycin) supplemented with LIF (10^3 unit/mL), FGFRi (1,5 μM) and Gsk-3i (1,5 μM) (LIF+2i condition). Medium was changed every day and cells were passaged every 2–3 days with 1X Trypsin-EDTA solution. Spinal motor neurons (MNs) were differentiated from mESCs HB9::GFP according to Wichterle et al.[77] and Errichelli et al.[78] After papain dissociation cells were plated on polyornithine/laminin-coated dishes with N2B27 medium (50% DMDM F12, 50% Neurobasal, 1X Glutamax, 1X Penicillin-Streptomycin, 1X B27, 1X N2, 200 ng/mL Ascorbic Acid, 20 ng/mL BDNF, 10 ng/mL CNTF, 10 ng/mL GDNF, 10 nM Rhok inhibitor) and differentiation was allowed to proceed for three additional days.

HeLa cells were cultured in Dulbecco's modified Eagle's medium supplemented with 2 mM L-glutamine, 100 U/ml penicillin, 100 lg/ml streptomycin, and 10% fetal bovine serum. Murine Neuro-2a cells (ATCC, Cat. No. CCL-131) were cultured in minimum essential medium Eagle (M2279, Sigma), supplemented with 2 mM L-glutamine, sodium pyruvate 1 mM, 1× MEM non-essential amino acid solution (M7145, Sigma), 1X Penicillin/Streptomycin (Thermo Scientific), 10% FBS premium USA sourced (45001-106, Corning).

For stress induction, cells were grown to 80% confluence and treated with 300 nM or 500 nM Tg for various time intervals as indicated.

Specific siRNAs were reverse transfected using Lipofectamine RNAiMAX (Thermo Scientific) according to manufacturer's instructions. Scramble and PDIA3 siRNA were purchased from Qiagen (AllStars Negative Control siRNA and FlexiTube GeneSolution GS14827 for Pdia3, respectively), while Lhx1os siRNA was custom-synthetized (Darmachon). siRNAs were used at a final concentration of 30 nM and sequences are listed in Table S4. Plasmid DNA transfection and plasmid DNA and siRNAs co-transfection were performed using Lipofectamine 2000 (Thermo Fisher Scientific) according to the manufacturer's specifications.

To achieve transcriptional inhibition, N2a cells were grown to 80% confluence and treated with actinomycin D (5 mg/ml) or DMSO for 8h, two hours before harvesting thapsigargin (500 nM) or DMSO were added. Prior RNA extraction a Spike RNA (10^7 copies) was added to each sample to allow normalization (Tataa Biocenter # RS25SI).

METHOD DETAILS

Lhx1os 5′RACE PCR

RACE PCR was performed using "FirstChoice® RLM-RACE Kit, Ambion, AM1700", following manufacturer's instructions on RNA obtained from Embryoid bodies at day 6 of differentiation. Oligonucleotides are available upon request.

Behavioral and functional tests

All experiments were conducted during the light phase of the light/dark cycle and only male mice were used. Before testing, animals were habituated to the testing room for at least 30 min. Mice that were tested in the open field, were tested 30 min later in the hanging steel task. A separate cohort of mice were tested in the treadmill exhaustion test. No blinding was done.

Open field test

The open field test was used to evaluate exploratory activity. During the open field task male mice were placed in the middle of a Plexiglas arena (40 × 40 × 40 cm). Animals were set free to explore the apparatus for 30 min. The distance travelled (m), the time spent in the periphery and the centre (s) and the maximum speed (m/s) were recorded using a video camera hanging over the arena that was connected to a video-tracking system (ANY-MAZE, Stoelting-USA).

Hanging steel test

After the open field test animals were tested in the hanging steel test to evaluate their grip strength. Animals were picked-up from the tail and their forelimbs gently placed on a suspended (40 cm) steel (2 mm diameter); when they gripped it, their tail was released and the latency to fall off the steel was recorded with a cut-off time of 120 s; two trials 30 min apart were performed, and the average was calculated for statistical analysis. The data were analyzed with a one-way ANOVA with the factors genotype (3 levels) as between group factor for the weight and distance travelled in the open field, and latency to fall in the hanging steel test.

Treadmill exhaustion test

The treadmill exhaustion test was performed according to Castro & Kuang,[36] with minor modifications. Briefly, P90 and P180 days old WT, HET and KO mice littermates were exercised to test their endurance. Mice were made to perform two 30-minute runs per week with increasing speed (10 cm/s for 10 min, followed by an increase of 1.5 cm/s every minute until a maximum velocity of 40 cm/s), for a total of 5 runs. If the mouse being tested stopped running, it received a small electric shock to stimulate further running until exhaustion (assessed after 5s of permanence on the electric grid). Total distance of the run, run time, n°of shocks and time of shock were recorded by the treadmill automated system (Panlab © 5-lane LE8710MTS). Before each run mice were habituated to the testing apparatus by a 5′ training run at 10 cm/s speed.

Motor neuron count

Spinal cords were dissected and fixed for 24 hours in 4% paraformaldehyde at 4°C and then immersed in 10%, 20%, 30% sucrose gradient, each passage until tissue sinking. Coronal 30 μm-thick cryosections of lumbar spinal cord (L1-L5) were cut sequentially and motor neurons were counted in at least 5 sections, spaced 180 μm each (n = 5 slices/animal; n = 3 animal per condition) by using Nissl/ChAT double staining. Sections were permeabilized in 1% BSA, 0.3% Triton for 1 hour at room temperature. Anti-ChAT primary antibody (AB144P; Millipore) was incubated in 1:100 dilution for 24 hours in the same solution. Neurotrace 500/525 Green Fluorescent Nissl stain (N21480) was incubated together with secondary antibodies for 1.30 hours in 0.01% BSA and 0.3% Triton. After washings with PBS, slides were incubated with DAPI (Sigma, D9542; 1ug/ml/PBS) to stain the nuclei. Slides were imaged using an inverted confocal Olympus IX73 microscope equipped with a Crestoptics X-LIGHT V3 spinning disk system and a Prime BSI Express Scientific CMOS camera. The images were acquired as 16 bit 2048x2048 pixel file by using a Plan CN 20X (NA 0,25) objective and were collected with the MetaMorph software (Molecular Devices). Semi-automatic quantification in post-acquisition analysis was performed using ImageJ software. No blinding was done.

MNs were identified as the Nissl+/ChAT+ cells in the ventral horn of the spinal cord with cell diameter > 20 μm in the P90 and P180 samples, as indicated in previous literature.[37,79] For the P7 samples, only the double- positive cells in the ventral horns were counted, independently of the cell area, according to the different size distribution of ChAT+ cells between postnatal and adult mice, as reported in previous literature.[41]

RNA-FISH and immunofluorescence

RNA FISH staining for Lhx1os was performed via Basescope™ assay (Advanced Cell Diagnostics, Bio-Techne) as described previously.[55,56] The specific probes set (cod. 716251) are custom designed to target the exon junctions of the three splice variants (Lhx1os 202/201/203).

Co-staining analyses were carried out by performing Immunofluorescence for KDEL and PDIA3 after FISH detection, by incubating the cells with primary antibodies (anti-KDEL monoclonal antibody 10C3, Enzo Lifesciences; anti-PDIA3 polyclonal antibody ab10287, Abcam) in 2% Donkey/Goat serum/PBS overnight

at 4°C. After extensive washing, cells were labelled with appropriate secondary antibodies (Goat anti-rabbit 488, Invitrogen A-11008; Donkey anti-mouse 647, Invitrogen A32787) in 1% goat serum/1% donkey serum/ PBS for 45 minutes at room temperature. The nuclei were counterstained with DAPI (Sigma, D9542; 1ug/ml/PBS) and the coverslips were then mounted using ProLong Diamond Antifade Mountant (ThermoFischer Scientific, P-36961).

SIM was performed using a N-SIM Super-Resolution Microscope equipped with a 1.49 NA 100x objective (Apo TIRF 100x Oil, Nikon, Tokyo, Japan) and with a 3D EX V-R 100x/1.49 Grating Block. Fluorescence was excited using a 4-laser unit equipped with 405, 488, 561 and 640 nm. SIM images were collected with NIS-Elements AR software (Nikon): ND acquisition module was used for 2x2 large image acquisition and stitching and for Z-stack (150 nm Z-spacing) images collection. The three reconstruction parameters illumination modulation contrast, high-resolution noise suppression and out of focus blur suppression were adopted to generate consistent Fourier tansforms. 3D-rendering and volume view of FISH-Immufluorescence stainings were performed with FIJI tools and NIS-Elements AR software (Nikon). The latter, were used also for Pearson's coefficient calculation, using the co-localization tool. Specifically, co-localization between Lhx1os and PDIA3 or KDEL was quantified as Pearson's correlation index on whole SIM-reconstructed ROIs or single confocal plane by JaCoP plug-in tool. Line-scan analysis were performed by FIJI software on maximum projection of Z-planes showing 3D-colocalized fluorescence signals.

For video-clip production Volume View and Movie Maker commands of NIS-Elements AR software (Nikon) were combined and applied on Z-stack (180 nm Z-spacing) images or on defined ROIs.

Mouse tissue collection for molecular analysis

Mice were weighed and then sacrificed by cervical dislocation. Relevant tissues were snap frozen in liquid nitrogen and stored at −80°C. Prior to protein or RNA extraction, tissues were ground to a powder using a pestle and mortar pre-chilled with liquid nitrogen. For protein extraction, tissue powders were homogenized using TissueRuptor II (QIAGEN) in RIPA buffer. The homogenates were centrifuged at 12,000xg for 10 minutes at 4°C and the supernatant was collected and quantified with the Bradford colorimetric reaction (Biorad).

Total RNA was isolated from tissue powder using QIAzol Lysis Reagent (Qiagen)/chloroform extraction followed by spin-column purification (RNeasy Mini Kit; Qiagen). 15′ minute on-column DNase treatment was performed, according to manufacturer's instructions. qRT-PCR detection was performed using PowerUp SYBR Green Master Mix (A25742, Life Technologies) on a 7500 Fast Real-Time PCR (Applied Biosystem) or Quant Studio 3^{TM} Real-Time PCR (Thermofisher). RNA expression, relative to GAPDH levels was analyzed through the $2^{-\Delta\Delta Ct}$ (Livak) Method.

RNA extraction and quantification by qRT-PCR

Total RNA was isolated from cell cultures using Directzol RNA MiniPrep (Zymo Research), and retrotranscribed with PrimeScript™ RT Reagent Kit (Takara Bio) according to the manufacturer's protocol, in a final reaction volume of 10 µL. qRT-PCR was performed using PowerUp SYBR Green Master Mix (A25742, Life Technologies). Relative RNA quantity was calculated as the fold change (2^{-DDCt}) with respect to the control sample set as 1, unless differently specified. Oligonucleotides used for qRT-PCR are provided in Table S4. DNA amplification was monitored with an ABI 7500 Fast qPCR instrument. Data analysis was performed using the SDS Applied Biosystem 7500 Fast Real-Time PCR system software.

Protein extraction and western blot

Whole-cell protein extracts were prepared from different types of cells using RIPA buffer. Western blot analyses were performed using NuPAGE SDS-PAGE (Invitrogen) or Mini-PROTEAN TGX (Bio-Rad) precast acrylamide gels according to the manufacturer's instructions, and proteins were transferred to Amersham Protran 0.45 µm nitrocellulose membrane (GE Healthcare Life Sciences) in 1× Towbin Transfer Buffer (25 mM TRIS, 192 mM glycine, 20% methanol). Membranes were blocked with 5% non-fat dry milk (Difco skim milk) for 1 h and incubated overnight at 4°C with the following primary antibodies: anti-LHX1 (PA5-78394, Invitrogen); anti-PDIA3 (ab10287, Abcam); anti-GAPDH (6C5, sc-32233, Santa Cruz Biotechnology). The following secondary antibodies were used: goat anti-rabbit HRP (31460, Invitrogen) and goat anti-mouse HRP (32430, Invitrogen). Protein detection was carried out with WesternBright ECL (Advansta) using ChemiDocTM MP System.

Overexpression constructs

The constructs for the overexpression of Lhx1os and PDIA3 were obtained by cloning cDNAs downstream the constitutive CMV promoter of the pcDNA3.1(+) vector (Addgene). Lhx1os was cloned between HindIII and NotI, while for PDIA3 the In-Fusion HD Cloning Kit (Clontech) was used. Oligonucleotides are listed in Table S4. The Lhx1osΔsi plasmid was generated, from the Lhx1os overexpression construct, by reverse PCR using the oligonucleotides listed in Table S4.

RNA antisense purification-mass spectrometry (RAP-MS) assay

RAP-MS assay was performed as described in McHugh et al.[48] on whole cell lysate derived from 20 millions of mESC-derived neural mixed population obtained from EB cells at day 6 that were dissociated and re-plated, allowing differentiation to proceed for additional 3 days (DIV3). Briefly, cells were UV-crosslinked using a Spectrolinker XL-1000 (0.8 Joules/cm2 of UV at 254 nm), scraped in Total Cell Lysis Buffer (Tris-HCl pH 7.5 10 mM, LiCl 500 mM, Dodecyl maltoside 0.5%, Sodium dodecyl sulfate 0.2%, Sodium deoxycholate 0.1%) and pelleted by centrifugation. Cell pellets were resuspended in cold Total Cell Lysis Buffer, passed 3–5 times through a 26-gauge needle, sonicated, added with 1X DNase salt stock and 20 U TurboDNase and incubated at 37°C for 10 minutes. DNA digested cells were returned on ice, added with 10 mM EDTA, 5 mM EGTA, and 2.5 mM DTT and supplemented with equal volume of 1.5X Hybridization Buffer (Tris-HCl pH 7.5 15 mM, EDTA 7.5 mM, LiCl 750 mM, Dodecyl maltoside 0.75%, Sodium dodecyl sulfate 0.3%, Urea 6M, DTT 3.75 mM), incubated 10 minutes on ice and pelleted by centrifugation. Supernatant was pre-cleared by incubation with washed streptavidin magnetic beads (Dynabeads MyOne C1) at 37 °C for 30 minutes with intermittent shaking. From the lysate, samples of 100,000 cells were collected, to obtain the RNA input sample. Pre-cleared lysate was mixed with 20 μg of biotinylated oligonucleotide probes and hybridized by incubating at 67 °C using an Eppendorf thermomixer with intermittent shaking for 2 hours. From the lysate, samples of 100,000 cells were collected, to obtain the RNA input + probe sample. Biotin-labeled RNP lysates were supplemented with streptavidin magnetic beads and incubated at 67 °C using an Eppendorf thermomixer with intermittent shaking for 30 minutes. Before the supernatant was discarded, samples of 100,000 cells were collected, this was the RNA flow-through sample. Probe-enriched RNP beads were washed 4 times for 5 minutes at 67°C with 1X Hybridization Buffer. 1% of the total beads were collected, to obtain the RNA elution sample. The remaining beads were resuspended in Benzonase Elution Buffer (Tris-HCl pH 8.0 20 mM, NLS 0.05%, MgCl2 2 mM, DTT 0.5 mM) together with 125 U of benzonase non-specific nuclease. Samples were incubated for 2 hours at 37°C with intermittent mixing. Beads were magnetically separated, and supernatant was transferred to a new microcentrifuge tube for 6 times to obtain the protein elution sample. RNA was eluted with NLS elution buffer (Tris-HCl pH 8.0 20 mM, EDTA 10 mM, NLS 2%, DTT 2.5 mM) and then extracted with Direct-zol RNA extraction kit (Zymo Reseach), for enrichment analysis by qRT-PCR. TCA-precipitated proteins were analysed by MS through Orbitrap ELITE/C18 Accucore 50 cm at the Plateforme de Protéomique, IGBMC (Illkirch, France). 90nt-long 5′-biotin modified DNA probes, antisense to Lhx1os or U1 snRNA, were purchased at Integrated DNA Technologies. Probe sequences are listed in Table S4.

Crosslinking immunoprecipitation (CLIP) assay

Cells were UV-crosslinked at 4,000 μJxcm^2 using a Spectrolinker UV Crosslinker, scraped in 200ul of NP40 lysis buffer [50 mM HEPES pH 7.5, 150 mM KCl, 2 mM EDTA, 1 mM NaF, 0.5% NP40, 0.5 mM DTT, complete EDTA-free protease inhibitor cocktail (Roche)], incubated for 15 min at 4°C on a rotating wheel and then centrifuged at 13,000 g for 10 min at 4°C. 2 mg of cellular extract for each sample (IP and IgG) were pre-cleared and 10% of input was collected. Pre-cleared extracts were incubated overnight at 4°C with 2ug of IgG or PDIA3 (anti PDIA3 polyclonal antibody ab10287, Abcam) specific antibodies and then coupled with Dynabeads Protein G magnetic particles at 4°C for 2h on a rotator. After washes with High Salt Wash Buffer (50 mM HEPES-KOH, 500 mM KCl, 0.05% NP40, 0.5 mM DTT, complete EDTA-free protease inhibitor cocktail) beads were resuspended in 200 μl of High Salt Wash Buffer. 50 μl (25%) were kept for protein fraction, resuspended in 30ul of 4× Laemmli sample buffer (Bio-Rad) and 50 mM DTT, incubated 15′ at 70° and analysed by Western blot. The remaining 150ul (75%) were diluted in 75ul of NP40 lysis buffer, treated with Proteinase K and incubated for 30′ at 50°C with shaking. RNA was extracted by miRNeasy Kit (Qiagen), retro-transcribed by Superscript Vilo cDNA synthesis Kit (11754050, Invitrogen) and analyzed by qRT-PCR using primers listed in Table S4.

RNA sequencing

Truseq Stranded mRNA was used to prepare cDNA libraries from Lhx1os +/+ and Lhx1os −/− spinal cord. Sibling mice were used. The sequencing reaction was performed on an Illumina Novaseq 6000 sequencing system at Istituto Italiano di Tecnologia (Genoa, Italy) and produced an average of 22 billion of 150 long paired end read pairs.

Quality of reads was assessed using FASTQC software (https://www.bioinformatics.babraham.ac.uk/projects/fastqc/).[80]

Novaseq6000 dark cycles during sequencing can lead to high quality Guanine stretches.

In order to remove these artifacts –nextseq-trim = 20 parameter of Cutadapt software were used.[81]

Illumina adapter remotion was performed using Trimmomatic software.[82] Reads that presented a length lower than 35 nt after trimming were filtered out.

Preprocessed reads were aligned to reference genome (GRCm38) using STAR (2.5.2b) aligner software[83] with specific parameters:

–outSAMstrandField intronMotif –outSAMattrIHstart 0 –outSAMtype BAM SortedByCoordinate –outFilterType BySJout –outFilterMultimapNmax 20 –alignSJoverhangMin 8 –alignSJDBoverhangMin 1 –outFilterMismatchNmax 999 –outFilterMismatchNoverLmax 0.04 –outFilterIntronMotifs RemoveNoncanonical.

After alignment Gene loci fragment quantification were performed on Ensemble (release 99) gene annotation gtf using htseq-count software[84] with these parameters: "-s reverse" and "-m intersection-strict".

Differential expression and gene ontology analyses

Differential expression analysis was performed with Deseq2 (version 1.30.0)[85] applying the Independent Hypothesis Weighting (IHW version 1.18.0);[86] genes with a *p*-value adjusted smaller than 0.1 were selected.

Gene ontology was performed by the webgestalt site (http://www.webgestalt.org)[87] using as method of interest the Over-representation analysis. For the down regulated genes both cellular component and biological process ontologies functional databases were used, while for the small number of upregulated genes, only the biological process with the noRedundant option was used. All genes expressed in both WT and KO samples (fpkms greater than zero) were used as background.

QUANTIFICATION AND STATISTICAL ANALYSIS

Data are shown as mean with s.e.m or mean with s.d. as indicated in the figure legends; the number of biological replicates is indicated in each Figure legend. Scatter-and-bar plots have been used to show individual biological replicate values. Box plots represent the 25th percentile, the median and the 75th percentile, while their error bars span from the minimum to the maximum value. Statistical tests used to assess significance of differences between means are indicated in each Figure legend. Significance values were depicted in the figures using the following key legend: *: $p < 0.05$, **: $p < 0.01$, ***: $p < 0.001$, ****: $p < 0.0001$. P-values < 0.05 were considered significant. GraphPad Prism was used for statistical test calculation.